February 2015

Detection of a Distinct Metal-Poor Stellar Halo in the Early-Type Galaxy NGC 3115*

Mark Peacock
Michigan State University

Jay Strader
Michigan State University

Aaron Romanowsky
San Jose State University, aaron.romanowsky@sjsu.edu

Jean Brodie
University of California Observatories

Recommended Citation

Mark Peacock, Jay Strader, Aaron Romanowsky, and Jean Brodie. "Detection of a Distinct Metal-Poor Stellar Halo in the Early-Type Galaxy NGC 3115*" *The Astrophysical Journal* (2015). https://doi.org/10.1088/0004-637X/800/1/13

The Astrophysical Journal, 800:13 (17pp), 2015 February 10 doi:10.1088/0004-637X/800/1/13

DETECTION OF A DISTINCT METAL-POOR STELLAR HALO IN THE EARLY-TYPE GALAXY NGC 3115*

Mark B. Peacock[1], Jay Strader[1], Aaron J. Romanowsky[2,3], and Jean P. Brodie[3]
[1] Department of Physics and Astronomy, Michigan State University, East Lansing, MI 48824, USA; mpeacock@msu.edu
[2] Department of Physics and Astronomy, San José State University, San Jose, CA 95192, USA
[3] University of California Observatories/Lick Observatory, Santa Cruz, CA 95064, USA
Received 2014 October 23; accepted 2014 December 8; published 2015 February 4

ABSTRACT

We present the resolved stellar populations in the inner and outer halo of the nearby lenticular galaxy NGC 3115. Using deep *Hubble Space Telescope* observations, we analyze stars 2 mag fainter than the tip of the red giant branch (TRGB). We study three fields along the minor axis of this galaxy, 19, 37, and 54 kpc from its center—corresponding to 7, 14, and 21 effective radii (r_e). Even at these large galactocentric distances, all of the fields are dominated by a relatively enriched population, with the main peak in the metallicity distribution decreasing with radius from [Z/H] ~ -0.5 to -0.65. The fraction of metal-poor stars ([Z/H] < -0.95) increases from 17% at 16–37 kpc to 28% at ∼54 kpc. We observe a distinct low-metallicity population (peaked at [Z/H] ~ -1.3 and with total mass $2 \times 10^{10} M_{\odot} \sim 14\%$ of the galaxy's stellar mass) and argue that this represents the detection of an underlying low-metallicity stellar halo. Such halos are generally predicted by galaxy formation theories and have been observed in several late-type galaxies, including the Milky Way and M31. The metallicity and spatial distribution of the stellar halo of NGC 3115 are consistent with the galaxy's globular cluster system, which has a similar low-metallicity population that becomes dominant at these large radii. This finding supports the use of globular clusters as bright chemodynamical tracers of galaxy halos. These data also allow us to make a precise measurement of the magnitude of the TRGB, from which we derive a distance modulus of NGC 3115 of $30.05 \pm 0.05 \pm 0.10_{\rm sys}$ ($10.2 \pm 0.2 \pm 0.5_{\rm sys}$ Mpc).

Key words: galaxies: abundances – galaxies: distances and redshifts – galaxies: formation – galaxies: halos – galaxies: individual (NGC 3115) – galaxies: stellar content – globular clusters: general

1. INTRODUCTION

The stellar halos of galaxies are relics of their past—preserved by their low densities and long relaxation times. As such, they provide key clues to their assembly history (Searle & Zinn 1978). The presence of extended low-metallicity stellar halos around all massive galaxies is a central prediction of hierarchical galaxy formation (e.g., Bullock & Johnston 2005; Cooper et al. 2010; Zolotov et al. 2010; Cooper et al. 2013). These halos arise naturally through the accretion and stripping of lower-mass galaxies and their entourages of globular clusters. The mass, metallicity, and density profile of a galaxy's halo are related to the number, size, and epoch of such interactions. The halo of a galaxy is, therefore, a prime location for understanding its past and for constraining galaxy formation in general.

Beyond the Local Group of galaxies, most of our knowledge of galaxy halos comes from surface brightness photometry of the integrated stellar emission (e.g., Martínez-Delgado et al. 2010; La Barbera et al. 2012; Mihos et al. 2013; van Dokkum et al. 2014; D'Souza et al. 2014). For example, Mihos et al. (2013) utilized such surface brightness photometry to probe the halo of NGC 4472 out to 7 effective radii (r_e), finding a color gradient that may be the result of the increasing contribution with radius of a low-metallicity stellar population ([Fe/H] < -1.0). However, most studies of galaxies using this method are limited to a few r_e and hence fail to probe the proposed accretion-dominated outer halo. This is because the extremely low surface brightness of the outer halos of galaxies limits the radii that can be observed with most telescopes. This work also requires extremely accurate sky subtraction and flat-fielding, making interpretation of observations challenging. In addition to these observational difficulties, integrated photometry can only determine the average properties of the stellar halo. Resolving the stellar populations of galaxy halos offers significantly more information but is necessarily limited to nearby galaxies.

The best-studied galaxy halo remains the Milky Way's, which is observed to have an old, smooth, and metal-poor stellar population (with mean [Fe/H] $= -1.6$ in the inner halo; Carollo et al. 2010). Resolved photometry of the stellar populations of the local and similar spiral galaxies NGC 891, M81, and M31 have shown that they also have a distinct metal-poor halo (Ibata et al. 2009; Monachesi et al. 2013; Ibata et al. 2014). In M31, this metal-poor halo has also been confirmed via spectroscopy of its red giant branch (RGB) stars (Gilbert et al. 2014). However, the well-studied stellar halo of M31 differs from the Milky Way in two important ways: first, in addition to an underlying old metal-poor population, there is a substantial population of higher-metallicity stars; second, a larger fraction of M31's halo is in clearly identifiable substructure.

Less data exist for the stellar halos of massive early-type galaxies. In pioneering work, the *Hubble Space Telescope* (*HST*) was used to study the stellar halos of the local early-type galaxies NGC 3115, NGC 3377, NGC 3379, and NGC 5128 (Elson 1997; Kundu & Whitmore 1998; Harris & Harris 2002; Rejkuba et al. 2005; Harris et al. 2007a, 2007b; Rejkuba et al. 2011)—initially finding only relatively enriched stars. It was only at much larger radii ($11 r_e$) that metal-poor stars started to emerge, although this was as a broad metallicity distribution in the halo of NGC 3379, rather than a distinct metal-poor population (Harris et al. 2007b). In recent work, more distant fields in NGC 5128 were observed by *HST* (Rejkuba et al. 2014). This showed a quite enriched halo

* Based on observations made with the NASA/ESA *Hubble Space Telescope*, obtained at the Space Telescope Science Institute, which is operated by the Association of Universities for Research in Astronomy, Inc., under NASA contract NAS 5-26555. These observations are associated with program #13048.

out to $25r_e$. However, the median halo metallicity did decrease with radius, and the outermost field was observed to have a higher fraction of metal-poor stars.

Another probe of a galaxy's halo is its globular cluster system. These star clusters are associated with major periods of star formation and are therefore thought to provide chemodynamical tracers of the underlying stellar populations of a galaxy. This is observed to be the case in the Milky Way and M31, where the metal-poor globular clusters are associated both spatially and chemically with the metal-poor halo population (see, e.g., the review of Brodie & Strader 2006). Globular clusters are particularly useful as probes of the stellar populations of galaxies because their relatively high surface brightness allows them to be accurately observed in relatively distant galaxies and at large galactocentric radii. These clusters can also contain a relatively large fraction of the stellar halo population of a galaxy—for example, 2% of the Milky Way's metal-poor halo mass is in its globular clusters, but these clusters only comprise 0.3% of the Galaxy's total mass.

The globular cluster populations of early-type galaxies are observed to have a strongly bimodal metallicity distribution (e.g., Peng et al. 2006; Strader et al. 2006), with the metal-poor globular clusters being more spatially extended than the metal-rich globular clusters (e.g., Bassino et al. 2006; Brodie & Strader 2006; Forbes et al. 2011). These observations suggest the presence of an underlying metal-poor stellar halo that extends to large radii around most early-type galaxies. However, direct detection of a distinct metal-poor stellar halo that corresponds to the metal-poor globular cluster population in early-type galaxies has proved challenging.

In this paper we present the stellar populations in the outer halo of NGC 3115—a nearby S0 galaxy at a distance of 10.2 Mpc (see Section 4) with $L_K = 9.5 \times 10^{10}\, L_{K,\odot}$ (Jarrett et al. 2003) and $r_e = 2.5$ kpc (Capaccioli et al. 1987).[4] Importantly, we observe this galaxy's halo at very large galactocentric radii—where any metal-poor halo should be more dominant. This galaxy is close enough to detect and resolve stars in its halo with *HST*, and it hosts a large and strongly bimodal globular cluster population (e.g., Brodie et al. 2012). As such, it is a prime location for observing an associated bimodal stellar halo population. Comparison with the galaxy's well-studied globular cluster population also provides a strong test of whether these globular clusters truly trace a galaxy's stellar halo.

The data used in this study are discussed in Sections 2 and 3. In Section 4 we use the tip of the red giant branch (TRGB) to determine the distance to NGC 3115. We discuss NGC 3115's stellar halo in Section 5, presenting its metallicity distributions (in Section 5.2) and radial profile (in Section 5.3). We conclude by comparing our observations with simple chemical enrichment models (Section 6), the halos of other galaxies (Section 7), and NGC 3115's globular cluster system (Section 8).

2. NGC 3115 OBSERVATIONS

We obtained *HST* observations of three fields in NGC 3115 between 2012 October and 2013 May under the program ID 13048 (P.I. Strader). The fields targeted, shown in Figure 1, were chosen to cover the regions of the galaxy where globular cluster

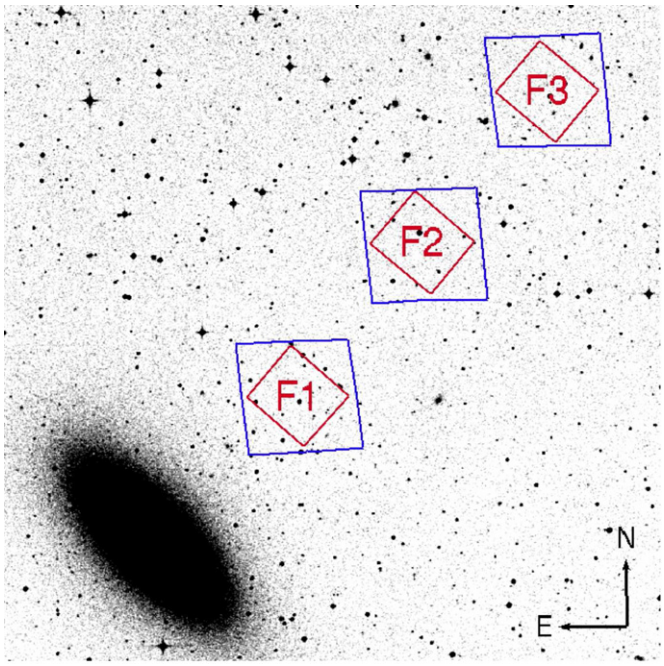

Figure 1. Fields of NGC 3115's halo that are covered by these ACS/WFC observations (large blue rhombuses) and WFC3/IR observations (smaller red diamonds). The image is taken from the Digitized Sky Survey 2 and covers $20' \times 20'$ on the sky. The fields F1, F2, and F3 are at galactocentric distances of 19, 37, and 54 kpc, respectively. This corresponds to $7r_e$, $14r_e$, and $21r_e$.

observations suggest that the stellar population may transition from being relatively metal-rich (in the inner field) to metal-poor in the outer field (Arnold et al. 2011). The observations were taken in coordinated parallel using the Advanced Camera for Surveys/Wide Field Camera (ACS/WFC) and the Wide Field Camera 3/Infrared Channel (WFC3/IR) through the F606W and F110W filters, respectively. The F606W is equivalent to a broad *V*-band filter, while the F110W spans the ground-based *Y* and *J* bands.

We utilize the pipeline-reduced flt images for each WFC3 exposure and the flc images for each ACS/WFC exposure, downloading them from the MAST archive[5] in 2013 August. Rather than utilizing the pipeline drizzle-combined images, we combine these flt/flc images together ourselves using the PYRAF/STSDAS/DRIZZLEPAC tasks TWEAKREG (to align the images) and ASTRODRIZZLE (to drizzle-combine all of the images together). We run these routines with the default parameters, with the exception of drizzle parameters final_pixfrac = 0.8 and final_scale = 0.0333 (for the ACS/WFC3) and 0.0666 (for the WFC3/IR). The resulting combined images of fields F1 and F3 have total exposure times in F110W and F606W of 18,240 s and 18,580 s, respectively. Field F2 has twice the exposure, with total exposure times in F110W and F606W of 36,480 s and 37,160 s, respectively.

3. PHOTOMETRY

We perform our primary photometry using the ACS and WFC3 specific modules of the DOLPHOT software (version 2.0, a modified version of HSTphot; Dolphin 2000). Rather than using the combined drizzled images for photometry, DOLPHOT is run using individual flt images, with the software using the drizzle-combined image only as a reference image. The

[4] This is the "bulge r_e" that was previously used to investigate the galaxy's globular cluster population (Arnold et al. 2011; Jennings et al. 2014). Along the minor axis of the galaxy $r_e = 1.7$ kpc (Capaccioli et al. 1987). The halo of NGC 3115 may have a lower ellipticity than the inner regions. We therefore choose the more circular "bulge r_e" but note that increased ellipticity places our fields at even larger r_e than quoted.

[5] http://archive.stsci.edu/

task performs point-spread function (PSF) photometry for each exposure and produces a combined magnitude for each source. This includes the required calibration, aperture corrections, and charge transfer efficiency corrections (for the flt images). We use the PSFs that are provided with the DOLPHOT software. These are from the TinyTim simulation with Anderson cores. Performing the photometry in this way is computationally more intensive. However, this method can potentially produce more accurate photometry and allows more accurate calculation of errors than using the drizzled images (where the drizzling process produces pixels with correlated noise).

To select only those sources with reliable photometry, we require the source to have the following DOLPHOT flags in both filters: object_type = 1 or 2, which selects stellar sources; error_flag $\leqslant$3; sharpness in the range −0.3 to 0.3, which helps to remove blended sources, background galaxies, and cosmic rays/detector artifacts; and crowding <0.3 mag, which removes sources whose photometry is significantly affected by neighbors. Stars are detected to 3.0σ detection limits of F606W = 29.7, 30.4, and 30.1 and F110W = 28.4, 28.9, and 28.5 in fields F1, F2, and F3, respectively. The resulting catalogs of sources in the F606W and F110W filters are combined based on their aligned World Coordinate System information using the software STILTS/TOPCAT (Taylor 2006).

We find that DOLPHOT's flags are not sufficient to remove all extended sources from our catalogs. We therefore use SEXTRACTOR to provide a better discrimination for marginally resolved sources. We run SEXTRACTOR over the drizzle-combined images and match the resulting catalogs to that produced by DOLPHOT. The colors and magnitudes are consistent between our SEXTRACTOR and DOLPHOT catalogs. To remove extended sources, we require that SEXTRACTOR's class_star flag be >0.5 in the F606W filter. This filter provides a better discriminant than the F110W filter, likely owing to the larger pixel size of the WFC3/IR and the shape of the IR PSF. We also remove extended sources by noting that point sources brighten by less than 0.5 mag from a 0.″15 to a 0.″3 aperture for the F606W filter and from a 0.″2 to a 0.″4 aperture for the F110W filter. Our final reduced (total) catalogs contain 4951 (13,914), 2335 (5295), and 549 (2126) sources for fields F1, F2, and F3, respectively.

The detection limits of these data in both filters can be estimated using DOLPHOT's artificial star tests. To do this, we place 40,000 stars in each image and perform the same photometry. For the artificial stars to be classed as detected, we require that the source is detected at >3σ and that the measured magnitude is within 0.5 mag of that input. Figure 2 shows the completeness function for each field through both filters. Field F2 is complete to fainter F606W and F110W magnitudes owing to the longer exposure time. For F110W, crowding is not important and the inner and outer fields (F1 and F3) have similar completeness limits. For the F606W observations, crowding results in field F1 having shallower detection limits than the outer field. For the F110W images, only 90%–95% of the artificial stars are detected in the brightest magnitude bin. Stars of this magnitude should easily be detected in these data. The missed sources are generally located close to bright sources, and this is the likely reason for their poor detection or nondetection. The incompleteness due to crowding does not have a color dependence that would significantly affect the derived metallicity distribution. Therefore, for our primary analysis of the RGB population, we are not concerned with spatial completeness and can scale the completeness functions so that the completeness in the brightest magnitude bin is 100%.

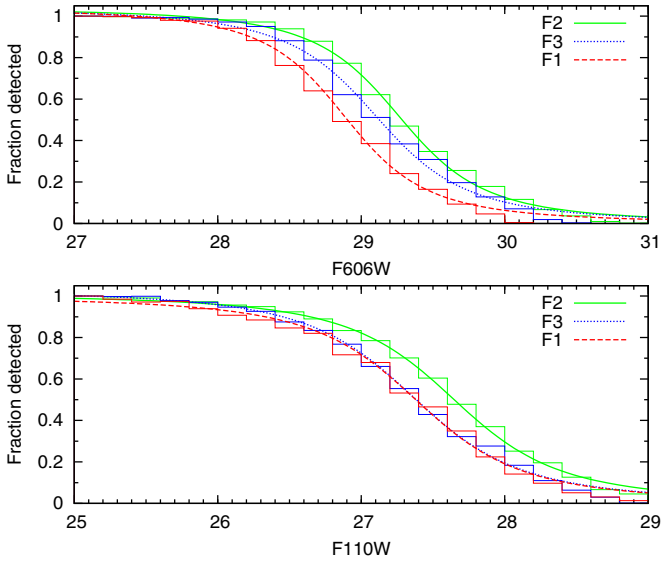

Figure 2. Fraction of artificial stars detected as a function of F606W (top) and F110W (bottom) magnitude. In both panels we plot the completeness in our three fields: F1 (red dashed line), F2 (green solid line), and F3 (blue dotted line). The curves are scaled to have a completeness of 1 in the brightest magnitude bin. As expected, the longer exposure time of the middle field (F2) results in slightly deeper detection limits. The outer field (F3) also reaches slightly deeper detection limits than the inner field. This is likely due to crowding effects. The curves are from fitting Equation (1) to the data.

The detection fraction is fit to a completeness function of the form

$$f = \frac{1}{2}\left(1 - \frac{\alpha(m - m_{50})}{\sqrt{1 + \alpha^2(m - m_{50})^2}}\right), \quad (1)$$

where m_{50} is the magnitude at which 50% of the sources are detected. The resulting 50% completeness limits are calculated as m_{50}(F110W) = 27.38, 27.64, and 27.36 and m_{50}(F606W) = 28.88, 29.26, and 29.10 for the fields F1, F2, and F3, respectively.

For analysis that relies on the distribution and total number of stars, such as the radial stellar density profile, we calculate two additional completeness corrections. Since the completeness is not constant across the images, primarily as a result of saturated stars and large background galaxies, we produce a spatial completeness map for each image. This is done based on our artificial star tests. Additionally, we note that our completeness correction is only valid for our DOLPHOT photometry. When matching to the SEXTRACTOR catalogs and removing galaxies, it is likely we also remove some stars. This is only found to be significant for the inner field, where crowding results in our star/galaxy separation being less reliable and rejecting some genuine stars. We correct for this by assuming that the number of background galaxies is constant across the three images and comparing this to the number of sources removed from the inner field.

3.1. Color–Magnitude Diagrams of NGC 3115's Halo

In Figure 3 we show the color–magnitude diagrams (CMDs) for all star-like sources, with reliable photometry, in the three halo fields of NGC 3115 (F1–F3 from left to right). The black dashed lines in this figure indicate the estimated 50% completeness limit for these data. The median errors are shown as a function of F110W magnitude. These errors are consistent

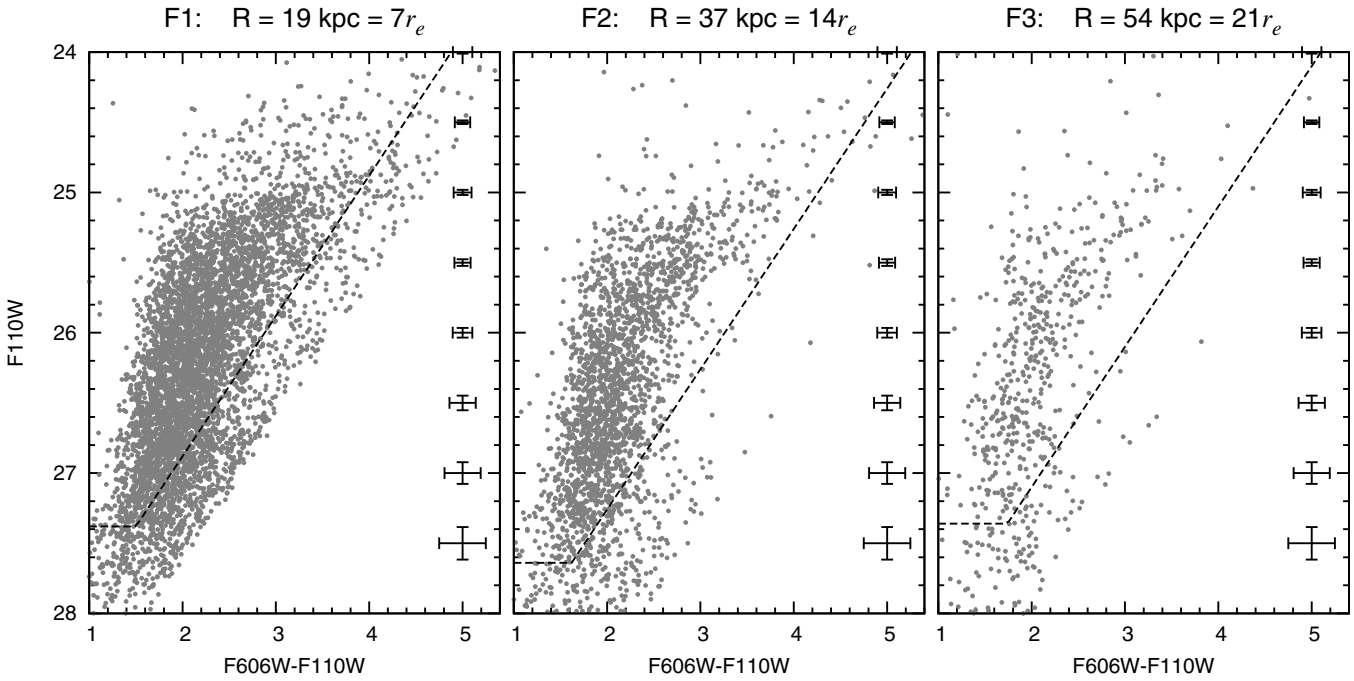

Figure 3. CMDs for star-like sources from the three fields in the halo of NGC 3115. The fields are located at galactocentric radii of 19 kpc ($7r_e$), 37 kpc ($14r_e$), and 54 kpc ($21r_e$), from left to right, respectively. The dashed line shows the 50% completeness limit.

with those estimated from our artificial star tests. It should be noted that, at fixed F110W magnitude, the uncertainty increases slightly for redder colors (owing to the source flux decreasing in the F606W filter).

As expected, the source density decreases sharply from the inner field (at $7r_e$) to the outer field (at $21r_e$). However, significant numbers of stars are detected in all three of the halo fields of NGC 3115. A rapid decrease in the density of sources is clearly visible for F110W $\lesssim$ 25.1. This region is associated with the TRGB. A small number of sources are observed above the TRGB. These can be explained as a combination of several different sources.

In crowded fields, the blending of sources can result in the detection of a single source brighter than the TRGB. Our halo fields are not very crowded owing to the quite low stellar density and the high spatial resolution of the *HST* images used. However, it is possible that some objects are still blended together. This effect will increase with stellar density—and hence the square of the number of stars. We estimate the influence of blending on our photometry using our artificial star tests. This confirms that blending is insignificant in the two outer fields (F2 and F3). In the inner field (F1), where the stellar density is higher, a tail of stars extending to 0.4 mag above the TRGB is observed in our artificial star tests. This is only a small fraction of the total number of stars in the field, but these blends may produce over half of the sources observed above the TRGB.

Some stars in NGC 3115's halo can have luminosities in excess of the TRGB, such as long-period variable (LPV) stars. These LPV stars are likely to be dominated by thermally pulsating asymptotic giant branch stars, but some variable RGB stars may also reach these magnitudes. Such bright stars are more prevalent in intermediate-age populations and will have relatively short lifetimes (e.g., Dalcanton et al. 2012). However, some of these stars should be present in an old stellar population (Renzini 1998), as is observed in old metal-rich globular clusters (e.g., Guarnieri et al. 1997; Lebzelter et al. 2014) and in other nearby galaxies (e.g., Harris et al. 2007a; Girardi et al. 2010). The number of these bright stars will scale with the size of the stellar population and hence the number of RGB stars.

There is also likely to be some contamination from foreground stars and (unresolved) background galaxies in the direction of our fields. Because our fields cover a similar area and direction on the sky, this background should be similar between the three fields. Using the Besançon model of the distribution of stars in the Milky Way (Robin et al. 2003), we expect only a few foreground stars in the magnitude and color range above the TRGB. Similarly, at these magnitudes, we would expect only a few unresolved background galaxies to be present (Radburn-Smith et al. 2011).

To estimate the relative contributions of these different bright sources to our three fields, we fit the number of stars observed above and below the TRGB to a function composed of a constant, representing contamination from foreground stars and background galaxies; a linear component, representing the LPV stars that scale with the number of RGB stars; and a component due to blending, which varies with the square of the number of RGB stars and is scaled to fit to the artificial star observations. We conclude that foreground stars/background galaxies may account for ~10 bright sources per field (consistent with the small numbers expected). The fraction of bright LPV stars to RGB stars (within 0.7 mag of the TRGB) is estimated at ~2.0% (consistent with the fractions observed in other galaxies by Girardi et al. 2010). The bright sources in the two outer fields (F2 and F3) are dominated by these bright stars and background contamination. The inner field (F1) contains more stars, and we find that blends may account for over half the bright stars observed, with LPV stars being the other significant component. We note that the number of bright stars in all fields is a small fraction of the number of RGB stars observed.

4. THE DISTANCE TO NGC 3115

Clearly visible in Figure 3 is a rapid decrease in the density of sources with F110W $\lesssim$ 25.1. This is associated with the TRGB and can be used to determine an accurate distance to

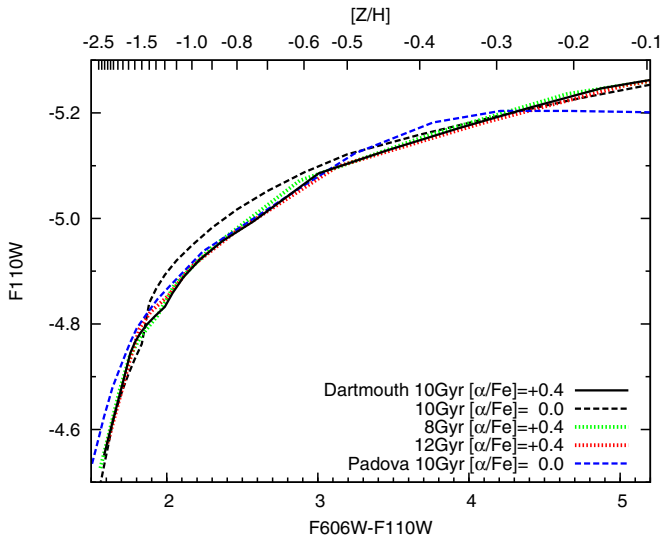

Figure 4. Absolute F110W magnitude of the TRGB as a function of color (and corresponding [Z/H] on the top axis). The solid black line is from the Dartmouth isochrones for a 10 Gyr old stellar population with $[\alpha/\mathrm{Fe}] = 0.4$. This is the model used to detrend the data in our TRGB analysis. We also plot curves for the same model but with $[\alpha/\mathrm{Fe}] = 0.0$ (black dashed line) and ages of 8 Gyr (green dotted line) and 12 Gyr (red dotted line). The dashed blue line shows a 10 Gyr stellar population from the Padova isochrones. It can be seen that no significant offsets are found between the different models or stellar populations; the age has little influence over the range 8–12 Gyr; the α-element abundance has a small effect (<0.05) that is largest at intermediate [Z/H]; and the Dartmouth values are in good agreement with the Padova values, with the largest difference (∼0.05) at the extremes of the metallicity distribution.

NGC 3115. The only previous TRGB distance to NGC 3115 was obtained from a single WFPC2 field. This was analyzed by two independent studies, which found the distance modulus to be 30.21 ± 0.25 (Elson 1997) and 30.19 ± 0.3 (Kundu & Whitmore 1998). The data presented in this study cover more area, are less crowded, and are much deeper than those of that previous study—this allows us to more precisely constrain the TRGB location.

4.1. The Absolute F110W Magnitude of the TRGB

A complication with using our data to measure a TRGB distance to NGC 3115 is that, in both the F606W and F110W filters, the magnitude of the TRGB varies as a function of metallicity—as opposed to previous work in the *I* band, where variations in the TRGB, as a function of metallicity, are relatively small (e.g., Lee et al. 1993). We take the TRGB magnitude in the F110W filter from the Dartmouth Stellar Evolution Database isochrones (Dotter et al. 2008) for a 10 Gyr stellar population with $[\alpha/\mathrm{Fe}] = 0.4$. We plot the TRGB as a function of [Z/H] in Figure 4. It can be seen that the TRGB increases by around 0.6 mag from $[\mathrm{Z/H}] = -2.2$ to $[\mathrm{Z/H}] = -0.1$. However, the predicted variation is similar for different models and model parameters. Only small variations in the TRGB magnitude are produced by altering the age of these models by ±2 Gyr, or the $[\alpha/\mathrm{Fe}]$ by 0.4. Additionally, good agreement is found between these Dartmouth isochrones and the Padova isochrones of Marigo et al. (2008; with age = 10 Gyr and $[\alpha/\mathrm{Fe}] = 0.0$). The absolute magnitude of the TRGB in F110W is quite poorly constrained empirically, and thus we rely on these model isochrones. For now, we estimate a systematic error on the TRGB magnitude of 0.1 mag (consistent with the uncertainties found by the near-IR TRGB study of Wu et al. 2014).

We choose the 10 Gyr Dartmouth isochrones with $[\alpha/\mathrm{Fe}] = 0.4$ to account for the variation in the TRGB as a function of F606W−F110W color. These parameters are consistent with those expected in NGC 3115's halo (see, e.g., the integrated spectroscopy out to 5 kpc along NGC 3115's minor axis; Norris et al. 2006). This model (and all those plotted in Figure 4) has been reddened to simulate the Galactic extinction in the direction of NGC 3115, where $E(B-V) = 0.042 \pm 0.001$ (Schlafly & Finkbeiner 2011). We use this model to correct the stellar photometry so that the TRGB is at F110W = −5 for all colors. The resulting CMD is plotted in the left panel of Figure 5. Here we combine the photometry from all three fields. We do not expect a significant change in the distance of the stars in the stellar halo and note that line-of-sight depth effects are insignificant since a depth of 20 kpc at this distance results in a magnitude variation of only 0.005. Therefore, combining these fields helps to increase the accuracy of our TRGB determination by increasing the sample size. Comparing this CMD to those in Figure 3, it can be seen visually that the TRGB is much more constant as a function of color—this verifies that the model isochrones used to detrend the data provide a good representation of the variation of the TRGB with color.

4.2. The TRGB in NGC 3115

To determine the TRGB location in this CMD, we run a Sobel filter over the luminosity function plotted in the middle panel of Figure 5. This filter is known to be a robust edge detection algorithm (see, e.g., Lee et al. 1993). We use an expanded version of the Sobel filter, which works by moving a filter of the form $[-p_{-2}, -p_{-1}, +p_{+1}, +p_{+2}]$ across the data. Here p_{-2}, p_{-1}, p_{+1}, and p_{+2} are the values 1 and 2 before and after the current value. In this way, flat distributions will cancel out and have a value of zero, while steep positive gradients produce a strong signal. The right panel of Figure 5 shows the response from this filtering as a function of magnitude. The strongest response is at F110W = 25.025. This is clearly associated with a sharp drop in the source density in the left panel and is taken to be the TRGB.

Our method for finding the TRGB relies on binning the data; a bin width of 0.05 mag is used. We experimented with using smaller bin sizes to increase our magnitude resolution, but the increased noise resulted in a weaker response from the Sobel filter. To investigate the accuracy of the TRGB magnitude obtained, we used a bootstrapping method. This method produces a new data set from our original data by randomly selecting entries from it (with replacement and equal probability) until the new data set is the same size as the original. We then rerun our analysis on the new data and measure the resulting TRGB. We repeat this process 10^5 times. The standard deviation of the resulting TRGB estimates from our bootstrapped runs is 0.05, and the mean is slightly shifted, with the TRGB at F110W = 25.048. This shift is likely due to the binning of the data, which limits our real data run to a 0.05 mag grid.

From this analysis, we take the TRGB to be at $\mathrm{F110W} = 25.05 \pm 0.05$. The data have been calibrated to define $\mathrm{M_{TRGB}} = -5.0$, with systematic errors due to the model used and stellar population effects estimated as ±0.1. We therefore obtain a distance modulus for NGC 3115 of $m - M = 30.05 \pm 0.05 \pm 0.1_{\mathrm{sys}}$ (or a distance of $10.2 \pm 0.2 \pm 0.5_{\mathrm{sys}}$ Mpc).

4.3. Comparison with Other Distance Estimates

Only two previous TRGB distances to NGC 3115 are available in the literature. These are from the same single WFPC2

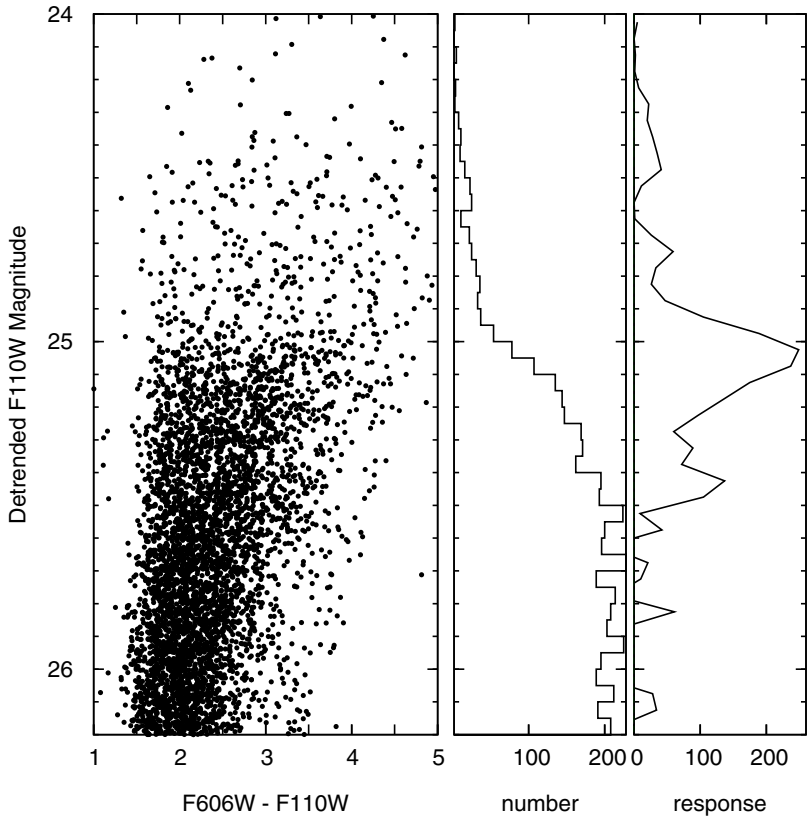

Figure 5. Left: combined CMD of all three fields studied. The F110W magnitude has been detrended so that the TRGB is constant as a function of color. This detrending appears to accurately represent the observed population, with a rapid decline in the density of sources with F110W $\lesssim 25$ clearly apparent. Middle: histogram of the number of sources at each magnitude (with 0.05 mag bins). Right: response from the Sobel filter—values of zero suggest a flat source density, while large values suggest a rapid increase in the number of sources. A peak is clearly apparent at F110W = 25.05.

observation and yielded consistent distance moduli of $(m - M) = 30.21 \pm 0.3$ (Elson 1997) and 30.19 ± 0.3 (Kundu & Whitmore 1998). Our measurement suggests a slightly closer distance but is consistent with these previous estimates. We note that our more precise measurement is due to the larger number of stars and lower crowding in our new observations.

Our derived distance is also consistent with other methods for deriving the distance to NGC 3115: planetary nebula luminosity function $m - M = 30.02 \pm 0.15$ (Ciardullo et al. 2002), surface brightness fluctuation $m - M = 29.93 \pm 0.09$ (Tonry et al. 2001), and globular cluster luminosity function $m - M = 30.00 \pm 0.07$ (Kundu & Whitmore 2001).

5. THE STELLAR HALO OF NGC 3115

5.1. CMDs of NGC 3115's Stellar Halo

In Figure 6 we again show the CMDs for all star-like sources, with reliable photometry, in the three halo fields of NGC 3115. The black dashed lines in this figure indicate the estimated 50% completeness limit.

Overlaid on these CMDs are the Dartmouth stellar isochrones for a distance modulus of 30.05 (see Section 4), an age of 10 Gyr, and [α/Fe] of +0.4. These parameters are consistent with those expected for a stellar halo population and are similar to those deduced from integrated spectroscopy of the galaxy's inner halo (Norris et al. 2006). We redden the isochrones to account for the Galactic reddening in the direction of NGC 3115, $E(B-V) = 0.042 \pm 0.001$ (Schlafly & Finkbeiner 2011). This reddening corresponds to extinctions of $A(\mathrm{F606W}) = 0.120$ and $A(\mathrm{F110W}) = 0.042$ (Cardelli et al. 1989). From left to right, these isochrones show [Z/H] from −2.2 to +0.2 in increments of 0.3 dex. We convert [Fe/H] to [Z/H] for these α-element-enhanced isochrones using Equation (3) of Salaris et al. (1993).

These isochrones, evenly spaced in metallicity, show the clear nonlinearity between color and metallicity. The metallicity has a much greater effect on the stellar colors at higher metallicities and luminosities. This causes the brighter metal-rich stars to fall beneath our detection limit. At low metallicity, the change in color is much smaller, and the stars bunch to similar colors. The result of this is that the CMDs can appear misleading, with the density of sources increasing artificially toward bluer colors.

The colors are clearly in excellent agreement with these isochrones for RGB stars in NGC 3115. We note that while the TRGB is clearly visible as a dramatic decrease in the number of sources, some sources with brighter magnitudes are detected. Many of these are likely to be AGB stars. We do not include the sources brighter than the TRGB in our subsequent analysis.

In Figure 7 we consider the effect of inaccuracies in the choice of isochrones used to represent the stellar population. For [Z/H] < -0.2, varying [α/Fe] from 0.0 (solar) to +0.4 has a negligible effect on the isochrones for constant [Z/H]. Similarly, varying the age of the stellar population from 8 Gyr to 12 Gyr has only a small effect on the isochrones. Finally, we consider differences between the Dartmouth (red solid line) and Padova (blue dashed line) isochrones. It can be seen that the two models produce very similar colors, with only small differences. We conclude that our analysis is relatively robust to the choice of model and our assumptions about the age and α abundance. Such effects are likely to produce systematic errors in the resulting metallicities of $\sim$0.1 dex. Since much

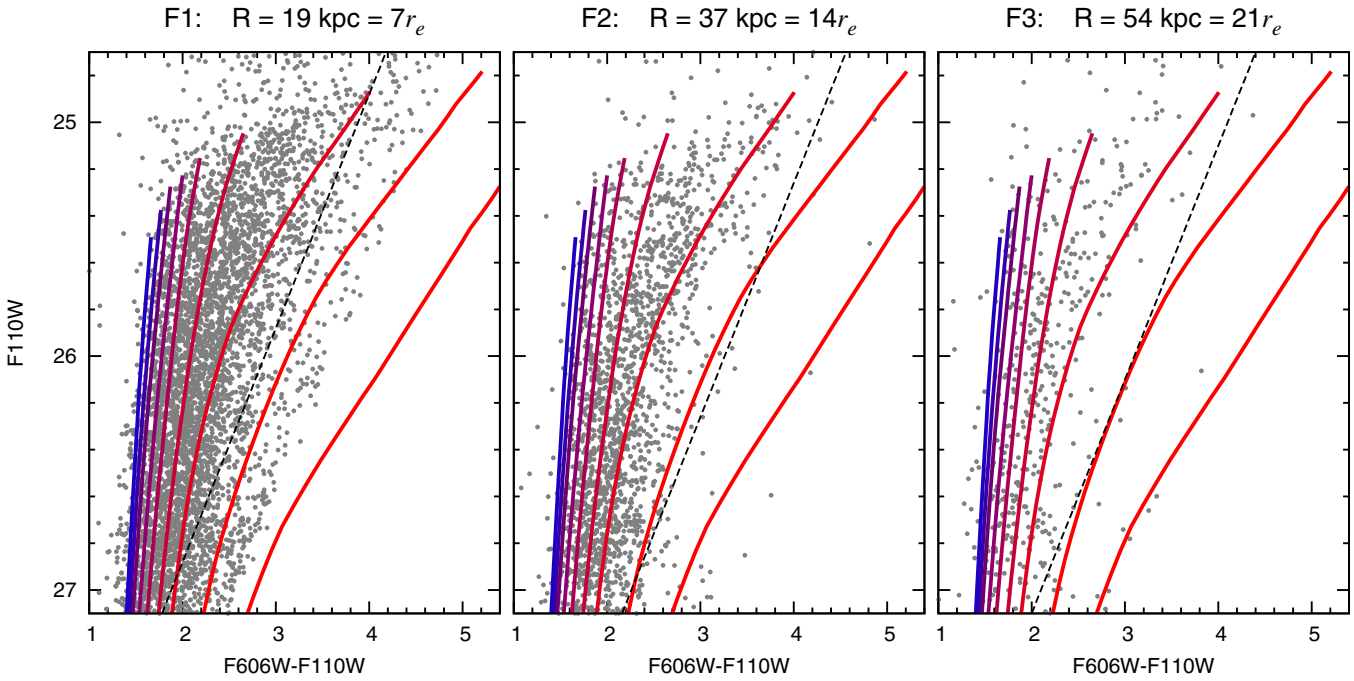

Figure 6. CMDs for our three fields. The dashed black lines indicate the 50% completeness limit. The solid lines are theoretical isochrones from the Dartmouth models. These show the tracks of a 10 Gyr stellar population with $[\alpha/\mathrm{Fe}] = +0.4$ and metallicities (from left to right and blue to red) of $[\mathrm{Z/H}] = -2.2, -1.9, -1.6, -1.3, -1.0, -0.7, -0.4, -0.1, +0.2$. The halo population is clearly in good agreement with these isochrones but spans the full metallicity range. The sources above the TRGB are likely AGB stars in the halo.

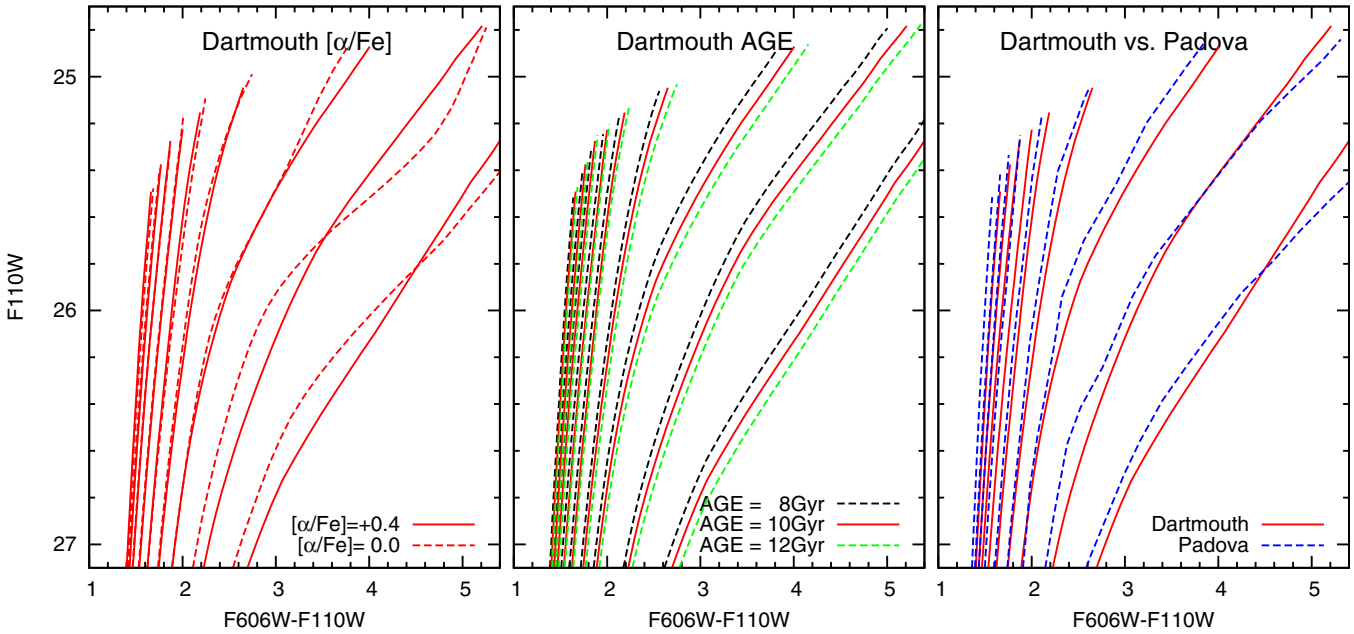

Figure 7. Comparison of isochrones with slightly different parameters. In all panels the solid red lines are the same isochrones as plotted in Figure 6. The dashed lines show isochrones with the same [Z/H] but with a varied second parameter. In the left panel we show the effect of changing the α abundance from +0.4 to 0.0 (solar). It can be seen that this has only a small effect. In the middle panel, we vary the age of the isochrones, showing 8 (black), 10 (red), and 12 Gyr (green). Again, at these old ages, such variations have only a small effect. The right panel compares the isochrones from the Dartmouth models and the Padova models. Good agreement is found between the different models. The differences observed are generally comparable to (or smaller than) the errors on our photometry.

of our analysis is comparative between the three radial fields, systematic errors will have little effect on our conclusions.

5.2. Metallicity Distribution of NGC 3115's Stellar Halo

The CMDs presented in Figures 3 and 6 can be used to investigate the stellar metallicity distribution function (MDF) in these three halo fields. To do this, we assume that the stellar population is well represented by the Dartmouth isochrones with an age of 10 Gyr and $[\alpha/\mathrm{Fe}] = +0.4$. We then match a star's CMD location to that of a grid of these isochrones separated in [Z/H] by 0.1 dex. As discussed above, small deviations in the age, α-abundance, and model used should only introduce small differences in the derived metallicities.

To improve the statistics, the goal is to include as many stars as possible in the derivation of the MDF. However, the increased errors and narrowing of the color difference with metallicity

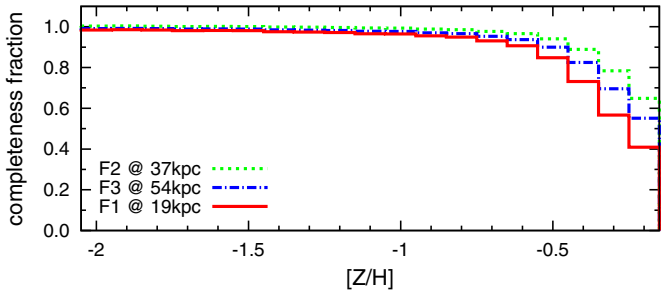

Figure 8. Completeness as a function of metallicity for stars with F110W < 26.5. The red solid line is for the inner field (F1), the green dotted line is for the middle field (F2), and the blue dot-dashed line is for the outer field (F3).

for fainter stars act to artificially smooth out the underlying MDF. The choice of magnitude limit is therefore nontrivial. In the Appendix, we investigate the MDFs produced using different magnitude cuts. While small variations are observed between the MDFs derived (see Figure 15), the key features are quite insensitive to these choices. In the subsequent analysis we consider all stars with F110W < 26.5. This simple cut allows us to consider a large number of stars with sufficiently accurate photometry.

Before studying the MDFs of NGC 3115's halo, we first calculate completeness corrections based on the artificial star tests discussed in Section 2. For stars with F110W < 26.5, this correction is shown in Figure 8. It can be seen that the completeness correction is only significant for [Z/H] > −0.4 and is largest for the inner field (where crowding lowers the detection of these relatively metal-rich stars). We correct the observed MDFs using these completeness corrections and restrict our analysis to stars with [Z/H] < −0.15 (because at higher metallicities the completeness corrections become increasingly large and unreliable).

Figure 9 shows the completeness-corrected MDFs for the three fields observed in NGC 3115's halo (centered at 19, 37, and 54 kpc from the center of the galaxy). The black and gray lines in this figure show the chemical enrichment models discussed in Section 6. It can be seen that all three fields are dominated by a quite enriched stellar population. The peak in the MDF shifts from [Z/H] ∼ −0.5 in the inner field to [Z/H] ∼ −0.6 in the outer field. We also note that the fraction of stars with high metallicity ([Z/H] > −0.4) is much lower in the outer two fields than in the inner field. We confirm this variation at the metal-rich end of the MDFs by running χ^2 tests between the three different fields over the range −0.95 < [Z/H] < −0.15. The resulting χ^2/ν statistics between the MDFs of fields F1–F2, F1–F3, and F2–F3, are 6.7, 16.6, and 7.8, respectively. For the eight degrees of freedom, this confirms that the MDFs at all three radii are significantly different at $>6\sigma$.

All three fields show a tail of stars extending to the lowest metallicities. We define a boundary between the metal-rich and metal-poor stars to be at [Z/H] = −0.95, based on the edge of the main metal-rich peak. The fraction of metal-poor stars is similar in fields F1 and F2 (centered at 19 and 37 kpc). For these fields, the metal-poor stars compose only 17% ± 1% and 18% ± 1% of the total population, respectively. However, the fraction of metal-poor stars in the outer field (F3, at 54 kpc) is significantly higher at 28% ± 3% of the total population.

A significant feature in the low-metallicity tails of the MDFs of fields F1 and F3 is a second peak at [Z/H] = −1.3 and [Z/H] = −1.25, respectively. The panels on the right of Figure 9 show a zoomed-in view of this section of the MDF. To estimate

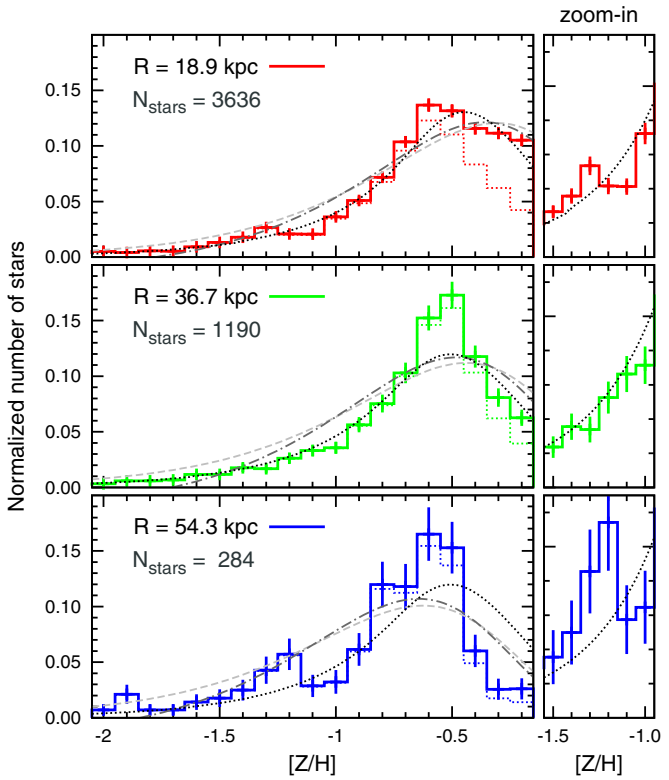

Figure 9. MDFs for the inner field (F1, top), middle field (F2, middle), and outer field (F3, bottom). The dotted histograms show the observed MDFs before correcting for completeness. The number of stars in each field is normalized to 1. The right panels show zoomed-in sections around the metal-poor peak. The error bars are the associated Poisson errors for each bin. In all fields a relatively metal-rich population with [Z/H] ∼ −0.5 is present. However, the peak of this population is found to shift to lower metallicities with increasing distance from the center of the galaxy. A second lower-metallicity peak can be seen in the tail of the distribution of fields F1 and F3 at [Z/H] ∼ −1.3. The dashed light gray, dot-dashed dark gray, and dotted black lines show model MDFs from a closed-box, a pre-enriched closed box, and an accreting gas model, respectively (see Section 6).

the significance of this peak, we compare it to the best-fitting accreting gas model (dotted black line; see Section 6). Over the region −1.45 < [Z/H] < −1.15, we find that this peak is 4σ above the model prediction for both fields F1 and F3. This peak is most pronounced in the outermost field, whose MDF has a significantly higher fraction of stars over the region −1.5 < [Z/H] < −1.0 than the other two fields (with a χ^2/ν of 7.8 and 7.5 with respect to fields F1 and F2, respectively, discrepant at $\sim 4.5\sigma$). The simplest explanation of this metal-poor peak is that it is the detection of a distinct metal-poor stellar halo that becomes an increasing fraction of the total population at larger radii.

For a smooth halo, the absence of the low-metallicity peak in the middle field is surprising. In Figure 10 we further investigate NGC 3115's halo by splitting the fields into radial bins (where the distance from the center of the galaxy increases from top to bottom). These MDFs now host similar numbers of stars (resulting in similar statistics). The general trends are still observed. In particular, the low-metallicity peak can still be seen in most of the inner fields despite the increased errors due to the lower number of stars in each MDF. This suggests that the absence of the low-metallicity peak in the middle field is not due to the lower number of stars compared to the inner field. Instead, the nondetection of the metal-poor peak is likely due to substructure. Such substructure is expected in galactic

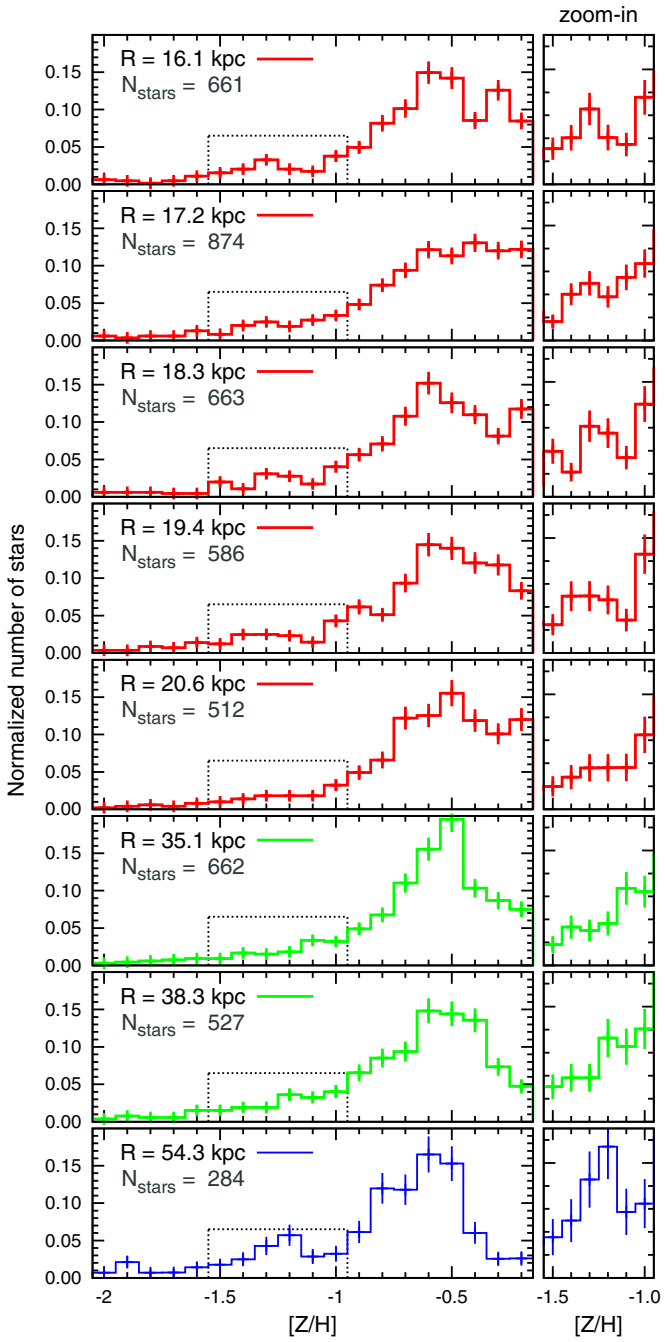

Figure 10. Same as Figure 9, but with the two inner fields split into radial bins. Distance from the center of the galaxy increases from top to bottom. Despite the increased noise, the low-metallicity peak is still observed in the four inner bins. In the middle field the low-metallicity peak is not observed at ∼35 kpc and the metal-rich population appears more peaked than in the other regions. Further out in this field at ∼39 kpc the metal-rich population broadens again and there are hints of the lower-metallicity peak. This is suggestive of substructure in the halo at R∼35 kpc. Despite having only half the stars of the other regions plotted, the outer field still shows the strongest low-metallicity population—a likely result of the ratio of metal-poor to metal-rich stars increasing with radius.

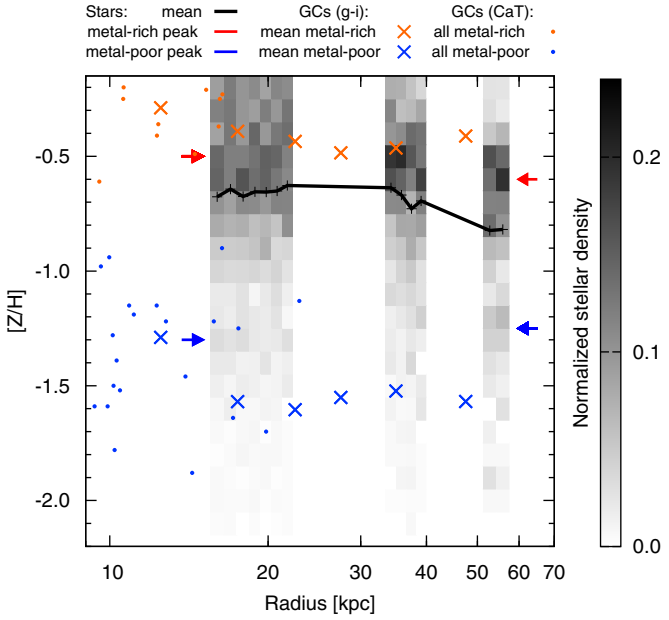

Figure 11. MDFs as a function of radius. Each radial bin is normalized to a total of 1 over the full metallicity range investigated ($-2.25 < [Z/H] < -0.15$). Darker bins represent a higher density of stars at that radius and [Z/H]. The MDFs are completeness corrected but truncated for $[Z/H] > -0.15$, where the correction becomes unreliable. The red and blue arrows indicate the locations of the metal-rich and metal-poor peaks in the inner and outer fields, respectively. The inner field has a broader metal-rich population and is clearly truncated at the metal-rich limit. At larger radii, the density of stars has dropped significantly before the metal-rich limit is reached. The black line tracks the mean [Z/H], which decreases from $[Z/H] = -0.65$ at 35 kpc to $[Z/H] = -0.8$ at 60 kpc. The orange and light-blue crosses show the mean metallicity of the metal-rich and metal-poor globular clusters, respectively, as determined from their integrated $g - i$ colors. The orange and light-blue points show individual clusters with metallicities determined from integrated spectroscopy. These globular clusters, as well as how they compare with NGC 3115's halo stars, are discussed in Section 8.

halos because of their long relaxation times. Interestingly, the outer region of field F2 does show hints of the low-metallicity population (though the reduced number of stars means that this is not significant). This suggests that we are observing some substructure in the inner regions of field F2 (at around 35 kpc).

Over/underdensities of metal-poor halo stars can be produced if these stars were accreted into the halo from the disruption of dwarf galaxies. Many dwarf galaxies are observed to have $[Z/H] \sim -1.3$ (e.g., Kirby et al. 2011, 2013), and their accretion and stripping can result in streams of metal-poor stars in the galaxy's halo. It is therefore possible that we do not detect the metal-poor peak in the middle field because it is underdense with respect to the inner and outer fields. This is consistent with Figure 12, which shows that the number of metal-poor stars, as well as the fraction of metal-poor to metal-rich stars, is lower than that expected at around 35 kpc (based on a power-law extrapolation of the other fields). Additionally, this field may have a slight overdensity of metal-rich stars with a more peaked metal-rich population than any other field (see Figure 10) and more metal-rich stars than expected ($\sim 2\sigma$ higher; see Figure 12). An overdensity of metal-rich stars makes it harder to detect the minority metal-poor population by hiding it in the tail of the metal-rich distribution. Such enriched streams have been observed in other galaxy's halos, most notably the Sagittarius stream in the Milky Way (Ibata et al. 2001b) and the giant stellar stream in M31 (Ibata et al. 2001a).

5.3. Trends with Galactocentric Radius

In Figure 11 we investigate the variation of metallicity as a function of radius in the halo of NGC 3115. In this figure the stellar density, as a function of radius and [Z/H], is indicated by the grayscale histogram, with higher-density regions having darker colors. The red and blue arrows show the metal-rich and metal-poor peaks observed in the inner and outer MDFs,

respectively. This figure highlights the trends observed in the MDFs: the fraction of stars with [Z/H] < -0.4 decreases significantly from 20 kpc to 60 kpc, and the higher-metallicity peak becomes slightly less enriched with increasing radius. In addition, the second peak in the MDF at around [Z/H] $= -1.3$ can be seen in many of the radial bins (with little radial variation). The black line in this plot traces the mean metallicity of the stellar population as a function of radius. This is found to decrease with increasing radius from [Z/H] $= -0.65$ to [Z/H] $= -0.8$. It should be noted that the mean metallicity at small radii ($\sim$20 kpc) may be slightly higher than calculated since the MDF at this radius is more truncated at our high-metallicity detection limit. This may artificially produce the observed flattening of the mean metallicity between 15 and 35 kpc. The orange and light blue points and crosses in this figure show the galaxy's globular cluster population (based on photometry from the catalog of Jennings et al. 2014). These clusters, as well as how they compare with NGC 3115's stellar population, are discussed in Section 8.

In the top panel of Figure 12 we show how the density of stars varies as a function of galactocentric radius for both the metal-rich stars ([Z/H] $\geqslant -0.95$, red points) and metal-poor stars ([Z/H] < -0.95, blue points). The metal-rich population, with a best-fitting power-law index of -3.0, falls off slightly more quickly than the metal-poor population, with a best-fitting power-law index of -2.7. This is consistent with a lower-metallicity stellar halo population that becomes increasingly important at larger radii. Assuming these power-laws fits, the halo will not be dominated by metal-poor stars until unrealistically large radii. However, there are suggestions that the metal-rich bulge/halo component may actually be falling off faster than this power law, with the outer field containing fewer metal-rich stars than expected. This is further demonstrated by the bottom panel of Figure 12, which shows that the fraction of metal-poor stars increases significantly in the outer field. In this panel we also show the effect that truncating the MDF may have on the metal-rich population at lower radii (as gray points). These points are generated under the assumption that 20% of the metal-rich stars are above our detection limit. Assuming this correction, the data are consistent with a much steeper power-law fit—such as the dotted gray line. Even assuming this fit, the low-metallicity stellar halo will not become the dominant component until $\sim$200 kpc.

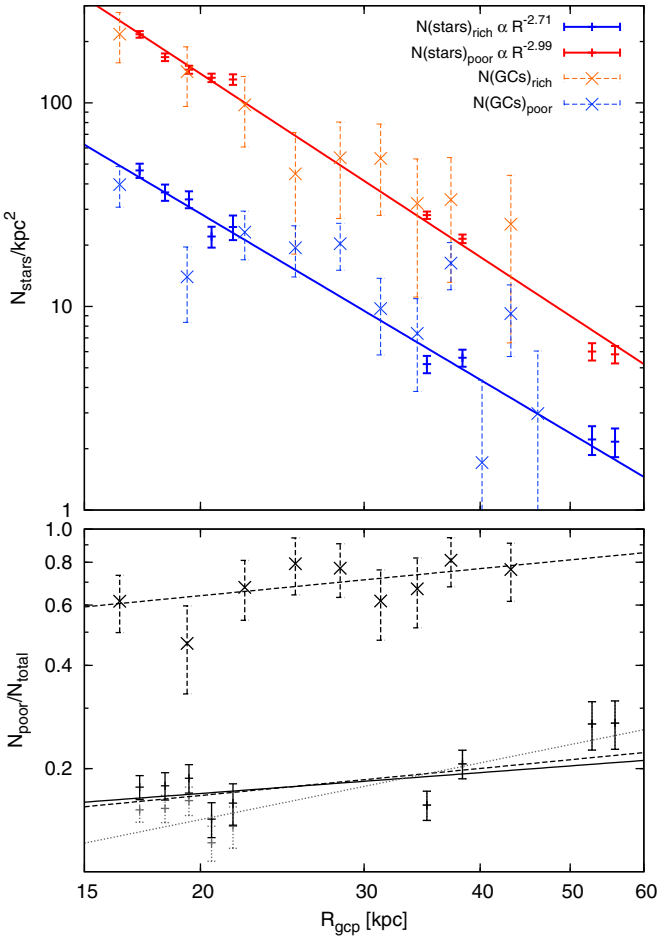

Figure 12. Top panel: projected density of stars and globular clusters as a function of radius from the center of NGC 3115. The dark blue points and light blue crosses show the metal-poor ([Z/H] < -0.95) stars and globular clusters, respectively. The red points and orange crosses show the metal-rich ([Z/H] $\geqslant -0.95$) stars and globular clusters, respectively. The best-fitting power laws to the metal-rich and metal-poor stellar populations are included. The globular cluster profiles are scaled to match the density of the corresponding stellar population. Bottom panel: fraction of metal-poor stars (points with solid error bars) and globular clusters (crosses with dashed error bars). The upper dashed black line is a power-law fit to the fraction of metal-poor globular clusters. The lower dashed black line is the same power law but scaled to fit the stellar population. The solid black line is a power-law fit to the fraction of metal-poor stars. The dotted gray line shows a power-law fit to the fraction of metal-poor stars, assuming a 20% increase in the metal-rich population in the inner field. The globular cluster results are discussed in Section 8.

5.4. The Mass of NGC 3115's Metal-poor Stellar Halo

The observed stellar density profiles, presented in Figure 12, allow us to estimate the total mass of NGC 3115's metal-poor stellar halo. The data provide a good constraint on the stellar density profile for $R > 15$ kpc but poorly constrain the shape of the profile at smaller radii. Because the stellar density profile is likely to flatten at small radii, we fit it to Sérsic functions, rather than the power law presented in Figure 12. We consider three profiles with Sérsic indices of $n = 2, 4$, and 8. All three profiles (and a power law) are consistent with the data. For each profile, we determine the total number of metal-poor stars (with F110W < 26.5) by integrating over all radii. We then convert this to a total stellar mass using a luminosity function from the Dartmouth models of Dotter et al. (2008; assuming a 10 Gyr old stellar population with [Z/H] $= -1.3$ and a Chabrier-like initial mass function). The derived metal-poor halo masses are $(1.1, 1.8, 3.9) \times 10^{10} M_{\odot}$ for $n = 2, 4$, and 8, respectively. This suggests that, for reasonable stellar density profiles, our estimate of the metal-poor stellar mass is accurate to a factor of $\sim$2.

We follow a similar method to estimate the total stellar mass of the metal-rich population. We conclude that, assuming a Sérsic index of $n = 4$, the total stellar masses of NGC 3115's metal-rich and metal-poor stellar populations are $M_{*,\mathrm{rich}} = 11.4 \times 10^{10} M_{\odot}$ and $M_{*,\mathrm{poor}} = 1.8 \times 10^{10} M_{\odot}$, respectively. This implies a stellar halo mass fraction of $\sim$14%. Lower fractions have been estimated for both the Milky Way ($\sim$2%; Bell et al. 2008; Cooper et al. 2013) and M31 ($\sim$4%, Courteau et al. 2011). The higher halo mass fraction estimated for NGC 3115 may be a result of differences in the evolution of early-type and late-type galaxies. The simulations of Cooper et al. (2013) produce a range of stellar halo mass fractions consistent with that estimated for NGC 3115.

We can also infer the total stellar mass of NGC 3115 from its integrated K-band luminosity (L_K). The K-band luminosity within 250″ (=12.3 kpc) has previously been estimated from

Two Micron All Sky Survey observations to be $L_K = 9.5 \times 10^{10} L_{K,\odot}$ (Jarrett et al. 2003). However, our observations demonstrate a significant stellar mass beyond 12.3 kpc. We therefore extrapolate this luminosity to include the stellar mass in the galaxy's outer halo, assuming the same profiles considered above (fit to the resolved stellar population). To convert to stellar mass, we take the mass-to-light ratio to be in the range $0.78 < M_*/L_K < 0.87$ (based on the integrated color of NGC 3115 and the relationship shown in Figure 1 of Fall & Romanowsky 2013). This implies a total stellar mass in the range $(9 < M_* < 17) \times 10^{10} M_\odot$—in excellent agreement with the total mass inferred from integrating our observed stellar densities, $M_* = 13 \times 10^{10} M_\odot$.

5.5. Summary: Properties of NGC 3115's Stellar Halo

Based on the MDFs presented in Figures 9–11, we note the key features of NGC 3115's stellar halo:

1. Across all three fields observed, spanning 15 kpc $< R <$ 57 kpc ($6r_e < R < 23r_e$), the stellar halo is dominated by a relatively metal-rich population—peaked in the range $-0.6 <$ [Z/H] < -0.5.
2. The main (metal-rich) peak in the MDFs becomes slightly less enriched with increasing radius, shifting from [Z/H] ~ -0.45 to [Z/H] ~ -0.65 from 15 to 55 kpc. Additionally, the fraction of high-metallicity stars (those with [Z/H] > -0.4) is much higher in the innermost field (F1) than in the two outer fields.
3. The mean [Z/H] drops with increasing radius from [Z/H] $= -0.65$ at 35 kpc to [Z/H] $= -0.8$ at 60 kpc. The inner region observed (15–35 kpc) has mean [Z/H] ~ -0.65 and shows no significant variation. However, the MDFs of the innermost regions are clearly incomplete, showing a significant fraction of stars up to our metal-rich detection limit.
4. All three fields show a tail of low-metallicity stars extending to the lowest metallicities. The fractions of metal-poor stars from 15 to 35 kpc are similar, composing 17% of the total population (although we note that the fraction may be lower in the innermost field because a larger proportion of its metal-rich stars are beyond our detection limit). The fraction of metal-poor stars in the outer field is significantly higher at 28%. A simple extrapolation of the population suggests that the galaxy's halo may not be dominated by metal-poor stars until $R \gtrsim 200$ kpc.
5. We observe a distinct metal-poor halo that is peaked at [Z/H] ~ -1.3. This is most pronounced in the outermost field. The detection of this metal-poor peak is consistent with an underlying low-metallicity stellar halo that is less concentrated than the metal-rich population.
6. There are hints of substructure in the halo at ~35 kpc.
7. We measure a total metal-poor stellar halo mass for NGC 3115 of $2 \times 10^{10} M_\odot$ and a total stellar mass of $13 \times 10^{10} M_\odot$.

6. COMPARISON TO MODEL MDFS

In this section we compare the MDFs of NGC 3115's stellar halo populations with the predictions from in situ star formation using three simple chemical evolution models: a pristine closed box, a closed box with pre-enriched gas, and an accreting gas model. We take these models in the forms presented by Kirby et al. (2011) and refer the reader to this paper (and the references therein) for more details. For all of these models we convert [Fe/H] to [Z/H] assuming the α-abundance used to derive NGC 3115's MDFs, [α/Fe] = +0.4.

6.1. Closed-box Model

In the closed-box model, initially pristine gas forms stars that feed metals into an isolated system. The gas is assumed to be well mixed at all times, and no material enters or leaves the system (see, e.g., Talbot & Arnett 1971; Binney & Merrifield 1998). This model predicts an MDF of the form

$$N \propto (10^{[\mathrm{Fe/H}]}) \exp\left(\frac{-10^{[\mathrm{Fe/H}]}}{p}\right). \quad (2)$$

Here p is the yield of each generation of stars (a measure of the fraction of heavy elements produced). To first order, this simple prediction provides a reasonable representation of the Milky Way's bulge population (e.g., Rich 1990). However, it predicts more metal-poor stars than are observed in the Milky Way's disk population, the long-known G-dwarf problem (as first proposed by van den Bergh 1962; Schmidt 1963) and later observed in both K dwarfs (Schlesinger et al. 2012) and M dwarfs (Woolf & West 2012). The G-dwarf problem has also been proposed based on the integrated properties of other galaxies (e.g., Worthey et al. 1996).

The gray dashed line in Figure 9 shows the best-fitting closed-box models to the three fields in the halo of NGC 3115. It can be seen that this model provides a poor fit to the data, predicting many more low-metallicity stars than are observed. We thus conclude that early-type galaxy spheroids may have a similar G-dwarf problem to the Milky Way's disk.

6.2. Pre-enriched Closed-box Model

A slight adaption to the simple closed-box model is to start the star formation from pre-enriched gas. The predicted MDF then takes the form

$$N \propto (10^{[\mathrm{Fe/H}]} - 10^{[\mathrm{Fe/H}]_i}) \exp\left(\frac{-10^{[\mathrm{Fe/H}]}}{p}\right). \quad (3)$$

Here the addition of the $[\mathrm{Fe/H}]_i$ term accounts for the initial metallicity of the gas. This condition may be expected if stars form from gas that was enriched by earlier star formation. For example, stars in the Milky Way's disk may have formed from gas enriched by prior star formation in the Galactic bulge. By predicting less metal-poor stars, this model provides a better representation of the Milky Way's disk stars. However, the model still predicts a larger metal-poor tail than is observed.

The best-fitting pre-enriched models to NGC 3115's halo MDFs are plotted as the dark-gray dot-dashed lines in Figure 9. This function produces an improved fit over the pristine closed-box model by reducing the number of metal-poor stars formed. However, the best-fitting models to the three MDFs all require high initial metallicities of $[\mathrm{Fe/H}]_i \sim -1.8$. Even allowing for this pre-enrichment, the model still provides a poor fit, predicting a less peaked MDF than observed.

6.3. Accreting Gas Model

In the accreting gas model, the system is allowed to accrete pristine gas over time. The model therefore requires less initial gas (from which the lowest-metallicity stars form). As the (pristine) gas is accreted, it mixes with the gas in the system (which is now enriched from earlier star formation) and

hence produces higher-metallicity stars. In this way, the model produces a stellar population with a lower fraction of metal-poor stars. Such a model provides a solution to the G-dwarf problem in the solar neighborhood (e.g., Pagel 1997; Prantzos & Silk 1998) and provides a good fit to the MDFs of the Milky Way's dwarf galaxies (Kirby et al. 2011).

We adopt the accreting gas model as presented by Kirby et al. (2011) (see also Lynden-Bell 1975, for the initial discussion of this model). In this model, the gas mass (g) is related to the stellar mass (s) via

$$g(s) = (1 - s/M)(1 + s - s/M). \quad (4)$$

The parameter M (>1) represents the amount of gas the galaxy accretes. The MDF of this model is given by

$$N \propto \frac{10^{[\mathrm{Fe/H}]}}{p} \frac{1 + s(1 - 1/M)}{(1 - s/M)^{-1} - 2(1 - 1/M)(10^{[\mathrm{Fe/H}]}/p)}, \quad (5)$$

where s is given by the equation

$$[\mathrm{Fe/H}](s) = log \left\{ p \left(\frac{M}{1 + s - s/M} \right)^2 \times \left[ln \left(\frac{1}{1 - s/M} \right) - \frac{s}{M} \left(1 - \frac{1}{M} \right) \right] \right\}. \quad (6)$$

We solve the equation for s numerically for a given [Fe/H] and M using the SCIPY task ROOT and perform a grid search to find the best accreting gas model fit to the observed MDFs. We consider parameters in the range $0.1 < M < 5.0$ and $0.1 < p < 0.5$. Similar fits were obtained to the three observed MDFs (in different radial bins). In Figure 9 we plot the best-fitting accreting gas model to the inner field (F1) as the dotted black line. This model has $M = 4.0$ (which is in the range determined for the Milky Way's dwarfs $1.3 < M < 9.1$; Kirby et al. 2011). This model provides a good representation of the MDF observed in field F1. The model also fits field F2 quite well, with the exception of the peak at [Z/H] $= -0.5$. This may again be suggestive of substructure in this middle field that produces the more peaked profile observed. The outer field, F3, hosts fewer metal-rich stars than predicted by this model, and the low-metallicity peak is clearly observed above the model prediction.

7. THE OUTER STELLAR HALO OF NGC 3115 AND OTHER GALAXIES

Previously, Elson (1997) studied an *HST*/WFPC2 field in the halo of NGC 3115. This field is ~22 kpc from the center of the galaxy, although it is closer to the major axis than our observations. Interestingly, this study also suggested a bimodal metallicity distribution in NGC 3115's halo with a metal-poor peak at [Fe/H] $= -1.3$ (slightly more enriched than observed in our fields, assuming a similar α-abundance). However, the implied MDF is quite different from our observations—theirs suggested similar numbers of stars in the metal-rich and metal-poor populations. It was also noted by Kundu & Whitmore (1998) that this bimodal distribution can be explained as an artifact of the WFPC2 calibration, which has a break between the two proposed populations. Given the relatively low fraction of stars we observe in the low-metallicity population, our results favor the interpretation of Kundu & Whitmore (1998)—that this field is likely dominated by a single population. However, it is possible that substructure may result in this field genuinely having a larger fraction of metal-poor stars. Additional *HST* observations, utilizing its updated instruments and covering a larger area, could resolve this question.

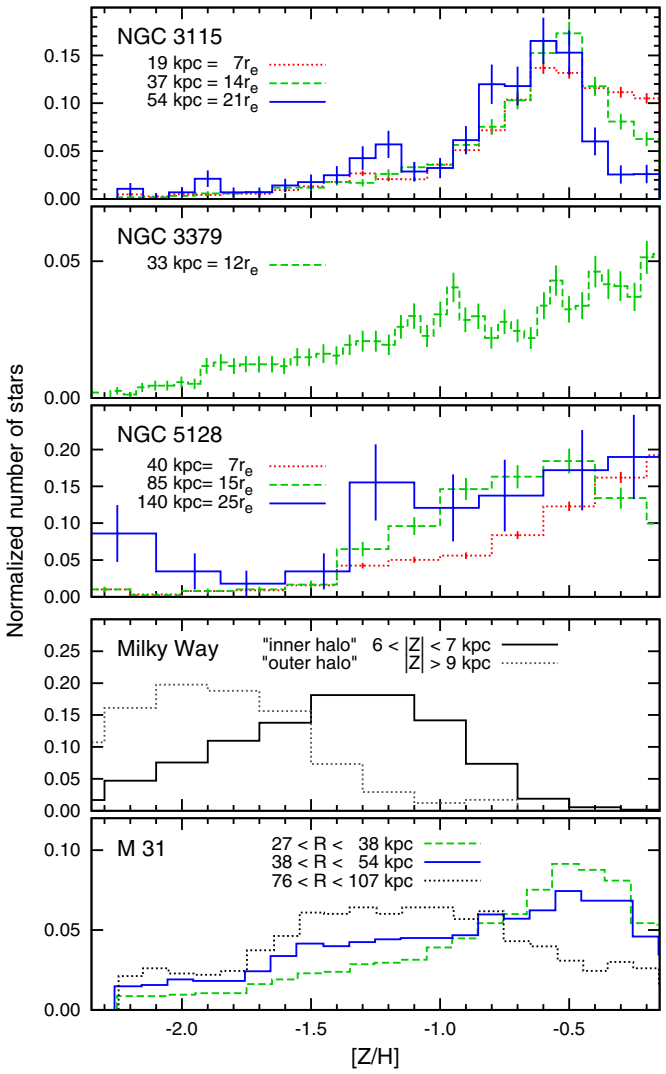

Figure 13. Outer-halo MDFs of local galaxies that have been investigated via their resolved stellar populations. The top three panels show the MDFs for the three early-type galaxies that have the *HST* observations required to resolve the stellar populations in their outer halos: NGC 3115 (this study), NGC 3379, and NGC 5128. The dotted red, dashed green, and solid blue lines show the MDFs at similar effective radii. The bottom two panels show the MDFs for two late-type galaxies, the Milky Way and M31. For M31, the dashed green and solid blue lines show MDFs at similar physical radii to those in NGC 3115.

Figure 13 compares NGC 3115's halo with that of other galaxies. Only two other early-type galaxies have *HST* observations of their halos at similarly large r_e. An ACS field $12r_e$ from the center of NGC 3379 was observed by Harris et al. (2007b). The derived MDF is shown in the second panel of Figure 13. A population of low-metallicity stars is observed, but this is part of a broader MDF than observed in NGC 3115. This observation was at similar radii to our middle field. The only early-type galaxy that has been observed at similarly large effective radii to our outer field (where the low-metallicity halo is likely to be most significant) is NGC 5128. Eight fields, four WFC3/UVIS plus four ACS/WFC (taken in parallel at a similar location), were observed in NGC 5128's halo from $10r_e$ out to $25r_e$ (Rejkuba et al. 2014). In the third panel of Figure 13 we

show the derived MDFs for three halo fields at similar r_e to our observations of NGC 3115. It can be seen that NGC 5128 has a broadly similar halo to that observed in NGC 3115, with the stellar population peaked at relatively high metallicity, the median metallicity reducing with increasing radius, and the fraction of metal-poor stars increasing in the outer field. In the outermost field of NGC 5128 there are also hints of the metal-poor peak that is observed at [Z/H] $= -1.3$ in NGC 3115's halo. However, the number of stars in this outer field (58) is significantly lower than that of our NGC 3115 analysis. This limits our ability to significantly test for this metal-poor population.

The properties of early-type galaxy halos, as inferred from integrated surface brightness photometry or spectroscopy, are normally limited to more central regions than probed by this study. However, several studies have pushed galaxy color profiles to quite large effective radii. For example, La Barbera et al. (2012) used the combined profiles of 674 early-type galaxies in the Sloan Digital Sky Survey to show clear color gradients out to $8r_e$. This color profile suggests that by $8r_e$ the galaxies have mean metallicities in the range $-1.0 <$ [Z/H] < -0.7. This range is consistent with the mean metallicity of NGC 3115's halo (see the black solid line in Figure 12). Recently, Mihos et al. (2013) used integrated photometry to trace (the early-type galaxy) NGC 4472's halo out to $7r_e$ (100 kpc). Interestingly, they identified a color gradient that, if purely due to metallicity variations, would imply a halo dominated by metal-poor stars with [Z/H] < -1.0. This halo would be quite unlike the one we observe in NGC 3115, which is dominated by significantly more enriched stars out to much larger r_e. It is interesting that these studies suggest that NGC 3115's halo is more enriched than these more massive galaxies at similar r_e. However, caution should be used when comparing galaxy halos based on similar effective radii, since these can correspond to very different physical radii. Future observations may be able to push to fainter surface brightness limits around more early-type galaxies (by using, for example, the dedicated Dragonfly telescope; Abraham & van Dokkum 2014). Such observations can cover a large fraction of a galaxy's halo and detect the stellar halo around relatively distant galaxies. They will therefore provide important complementary data to *HST* observations of the resolved stellar population.

The fourth panel of Figure 13 shows the Milky Way's inner-halo ($6 <$ |Z| < 7 kpc) and outer-halo (|Z| > 9 kpc) MDFs as measured by Carollo et al. (2010; and converted to [Z/H] assuming [α/Fe] $= +0.3$). It can be seen that NGC 3115's halo is markedly distinct from the Milky Ways (which is dominated by metal-poor stars at similar radii). However, caution should be used when directly comparing the halo of NGC 3115 with that of the Milky Way (a late-type galaxy with little evidence of a bulge contribution to its halo). It should also be noted that the Milky Way's halo may not be typical of all spiral galaxies. Indeed, the presence of a low-metallicity population in M31's halo was only clearly identified with resolved stellar photometry (Ibata et al. 2014) and spectroscopy (Gilbert et al. 2014) of a large fraction of its halo to beyond 100 kpc.

In the bottom panel of Figure 13 we also show the MDFs of M31's halo within three radial bins (taken from Ibata et al. 2014). Over the range 20–100 kpc the halo MDF shifts to lower metallicities. However, the lower-metallicity population only becomes dominant at much larger radii than in the Milky Way's halo—beyond ~70 kpc. Additionally, some regions of M31's outer halo are more enriched than the MDFs shown (which exclude regions of spatially distinct higher-metallicity stars, most notably the giant stellar stream; Ibata et al. 2001a, 2014). At a similar physical radius to the outer observation of NGC 3115's halo, M31's halo has a larger fraction of metal-poor stars but is otherwise remarkably similar (with metal-rich and metal-poor populations peaked at [Z/H] ~ -0.6 and [Z/H] ~ -1.3). We again note that caution should be used when comparing early- and late-type galaxies, but it can be seen that M31's halo is not dominated by metal-poor stars until $\gtrsim$70 kpc, which is more distant than we observe in NGC 3115.

8. TRACING STELLAR HALOS WITH GLOBULAR CLUSTERS

As bright chemodynamical tracers of the stellar population of a galaxy, globular clusters are thought to be powerful probes of the outer halos of galaxies (where their stellar populations are often challenging/impossible to observe directly). The observations presented here allow us to directly compare the stellar halo of NGC 3115 with inferences from the galaxy's globular cluster system.

The globular cluster systems of early-type galaxies have two key features that provide clues to the stellar population of their halos. Firstly, it is well established that the globular cluster populations of most galaxies have a bimodal metallicity distribution with a metal-rich population peaking at [Z/H] ~ -0.5 and a metal-poor population peaking at [Z/H] ~ -1.5 (e.g., Peng et al. 2006; Strader et al. 2006). Second, it has been observed in many galaxies that the metal-poor clusters are more spatially extended than the metal-rich clusters (e.g., Bassino et al. 2006; Brodie & Strader 2006; Forbes et al. 2011). An interpretation of these two common properties of globular cluster systems is that most galaxies have a distinct, extended, low-metallicity stellar halo that extends to many effective radii and is associated with the metal-poor globular cluster population. However, this interpretation is poorly tested, particularly in early-type galaxies.

NGC 3115 has a large globular cluster system with a strongly bimodal MDF (e.g., Arnold et al. 2011; Brodie et al. 2012; Cantiello et al. 2014; Jennings et al. 2014). The metal-poor clusters are observed to be less centrally concentrated than the metal-rich clusters, with the ratio of low- to high-metallicity clusters increasing with radius (e.g., Arnold et al. 2011). In the top panel of Figure 14, we plot the MDFs of NGC 3115's globular cluster system based on *HST* observations and the suite of data available from the SLUGGS survey (Brodie et al. 2014). The black dashed line shows the globular cluster MDFs from spectroscopic observations utilizing the CaT index (sensitive to the Ca II triplet; Brodie et al. 2012). These data cover a sample of clusters out to a radius of 20 kpc. We also consider the MDFs based on the recent globular cluster photometric catalog of Jennings et al. (2014). The purple dotted line shows the MDF based on *HST* observations of the inner region of the galaxy ($\lesssim$15 kpc), converted from $g-z$ color to [Z/H] based on the empirical relationship of Peng et al. (2006). The gray solid line shows the MDF based on $g-i$ color from Subaru/Suprime Cam observations, converted to [Z/H] based on the conversion presented in Usher et al. (2012). These data cover clusters out to larger radii ($\lesssim$50 kpc). However, without high-resolution imaging or spectroscopic confirmation, there is likely to be more contamination from noncluster sources in these data.

It can be seen that all measurements show the globular cluster system to be strongly bimodal. However, the peak of the metal-rich and metal-poor populations varies slightly between the different measurements, with peaks in the range $-0.5 <$

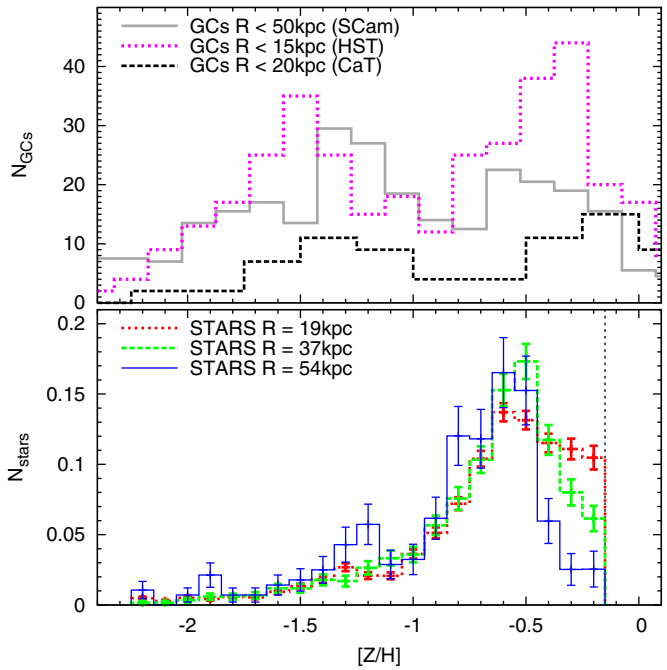

Figure 14. MDFs of NGC 3115's globular cluster population (top) and stellar halo population (bottom). The different lines in the globular cluster MDFs show [Z/H] as inferred from spectroscopy of a sample of clusters out to 20 kpc (dashed black), $g-z$ color from *HST* observations out to 15 kpc (dotted pink), and $g-i$ color from ground-based observations out to 50 kpc (scaled to $N_{GCs}/2$; solid gray). The stellar MDFs are as in the previous figures and are centered at 19 kpc (dotted red), 37 kpc (dashed green), and 54 kpc (solid blue).

[Z/H] < -0.2 and $-1.5 <$ [Z/H] < -1.3, respectively. Some of this variation may be attributed to radial variations, since the globular cluster peaks may become bluer with increasing radius (see Figure 11 and Jennings et al. 2014). However, variation may also be due to systematic errors in the methods used to convert color and spectroscopic index to [Z/H]. This is a particular issue for the metal-poor clusters where metallicity variations result in only small color variations. We adopt a metallicity of [Z/H] $= -0.7$ as the boundary between the metal-rich and metal-poor globular clusters. This is similar to the boundary adopted by Jennings et al. (2014) and provides a good split between the two peaks observed in the globular cluster MDFs (see Figure 14). However, this is slightly more enriched than the boundary chosen for the stellar population ([Z/H] $= -0.95$). We choose to keep these different boundaries and note that some of this offset may result from the relatively small fraction of metal-poor stars. The effect of this is that the MDF is dominated by the tail of the metal-rich population to relatively low metallicities.

The bottom panel of Figure 14 shows the MDF of the three stellar halo fields presented in this paper. The MDFs of these fields have metal-rich peaks in the range $-0.6 \lesssim$ [Z/H] $\lesssim -0.5$. This is similar to the metal-rich globular cluster population, though perhaps offset to lower metallicities by 0.1–0.2 dex. Some of this shift may result from the larger galactocentric radii of the stellar halo populations relative to the majority of these globular clusters. Indeed, it can be seen from Figure 11 that, in a similar fashion to the stellar population, the metal-rich globular clusters become less enriched with increasing radius (as inferred from their integrated $g-i$ colors). Based on comparing the integrated colors of galaxy bulges with their globular cluster colors, Spitler (2010) have previously proposed that the metal-rich globular clusters may be slightly less enriched than the stellar bulge stars of massive galaxies. For a galaxy with the mass of NGC 3115,[6] their work suggests that the metal-rich globular clusters may be less enriched by ∼0.2 dex. Our data are consistent with such a shift. However, we also note that this offset could be produced by systematic uncertainties in the different methods used to estimate metallicity (stellar CMD fitting for the stars relative to stellar population fitting to integrated colors/spectral indices for the globular clusters). This is evident from the top panel of Figure 14, where similar-sized offsets can be seen between the metal-rich peaks of the globular cluster population derived from different methods. Further investigation of the metallicities derived from these different methods is clearly important but is beyond the scope of this paper.

Figure 14 also shows that the second, lower-metallicity peak observed in the stellar halo is at a similar metallicity to the peak of the metal-poor globular clusters. This peak is likely the detection of the metal-poor stellar halo of NGC 3115, which is associated with its metal-poor globular clusters. We note that, based on their $g-i$ colors, the metal-poor globular clusters may shift to lower metallicities at larger radii (beyond 15 kpc). This can be seen in Figure 11, where the mean metallicity of the metal-poor globular clusters decreases from [Z/H] ~ -1.3 at small radii to a constant [Z/H] of ~ -1.6 from 20 to 50 kpc. The peak of the metal-poor stellar halo shows a similar lack of radial variation over 20–50 kpc but is more enriched by ∼0.3 dex. We again note that this shift might be explained by errors in the conversion of stellar CMDs and integrated color to metallicity. This is a particular issue at these lower metallicities, where variations in metallicity result in relatively small variations in color.

In Figure 12 we show the radial profiles of NGC 3115's metal-rich and metal-poor globular clusters (as orange and light-blue crosses, respectively) and stars (as red and blue points, respectively). These globular cluster profiles were produced using the Subaru/Suprime Cam photometry, published in the catalog of Jennings et al. (2014). It is likely that a significant fraction of these globular cluster candidates in the outer regions are misclassified background galaxies. We estimated this background for both the metal-rich and metal-poor clusters based on the density of sources in the outermost regions (∼60 kpc). The globular cluster profiles were then scaled to fit the number of stars in the corresponding stellar population. Owing to the lower number of sources, the globular cluster profiles have significantly larger errors than the stellar profiles. However, it can be seen that the radial profile of NGC 3115's globular clusters is consistent with the galaxy's halo stars. Specifically, it can be seen that metal-rich globular clusters have a steeper profile than the metal-poor globular clusters, as observed in the stellar populations. This is highlighted by the bottom panel of Figure 12, where the fractions of metal-poor globular clusters and stars are observed to increase with increasing radius.

The major difference observed between the stellar and globular cluster populations is that the fraction of metal-poor stars in the halo of NGC 3115 is much smaller than the fraction of metal-poor globular clusters. This can be seen in the bottom panel of Figure 12, which shows the fraction of metal-poor globular clusters and stars. For both populations, this fraction increases with radius. However, the fractions are very different. A similar difference is observed in the Milky Way,

[6] $M = 8.2 \times 10^{10} M_{\odot}$, based on its K-band luminosity ($L_K = 9.5 \times 10^{10} L_{K,\odot}$; Jarrett et al. 2003) and assuming $M/L_K = 0.86$ (as used by Spitler 2010).

where 70% of its globular clusters are associated with its metal-poor halo (e.g., Bica et al. 2006), but the Milky Way's metal-poor halo composes only ∼2% of its total stellar population (Carollo et al. 2010). The fraction of metal-poor globular clusters is also observed to be much higher than the fraction of metal-poor stars in the outer halo (>8 kpc) of NGC 5128 (Harris & Harris 2002). Harris & Harris (2002) also calculate the specific frequency of NGC 5128's globular clusters (S_N, a measure of the number of GCs to a galaxy's V-band luminosity) as a function of metallicity. They find that S_N increases with decreasing metallicity. From the stellar and globular cluster density profiles presented in Figure 12, we calculate that the specific frequency of the metal-poor population in NGC 3115's halo is 7.5 times higher than that of the metal-rich population. The reason for this difference is currently uncertain. It may suggest that, in metal-poor environments, relatively more stars form in larger, denser clusters. Or it may be that clusters experience less destruction in these metal-poor environments (perhaps because they originate in dwarf galaxies that then accrete into the halos of these higher-mass galaxies).

Our observations of NGC 3115's stellar and globular cluster populations present a consistent picture of the galaxy's halo. They both suggest a metal-poor stellar population, peaked at [Z/H] ~ -1.3, that is more spatially extended than a more enriched population, with [Z/H] ~ -0.5. We note that the major difference between the stellar and globular cluster populations is in the ratio of the metal-poor to metal-rich stars/clusters, which is much smaller for the stellar population.

The MDF and radial profile of NGC 3115's globular cluster population are consistent with its observed stellar halo. This supports the use of globular clusters as tracers of the stellar populations of early-type galaxies. Our conclusions are consistent with the findings of other studies that have shown that, out to a few r_e, the metal-rich globular clusters have similar metallicities to those of early-type galaxies stellar populations, as inferred from their integrated colors (Spitler 2010) and spectra (N. Pastorello et al., in preparation).

9. CONCLUSIONS

We use deep *HST* photometry to study the outer halo of the early-type galaxy NGC 3115. These observations detect and resolve thousands of the galaxy's RGB stars, 2 mag beneath the TRGB. The TRGB is obvious in these data, and we measure a TRGB distance modulus for NGC 3115 of $30.05 \pm 0.05 \pm 0.10_{\rm sys}$—where the calibration of the TRGB magnitude through the F110W filter dominates the uncertainty.

By comparing to the Dartmouth stellar isochrones, we produce MDFs of NGC 3115's halo over the range 15–60 kpc (6–23r_e). We show that, even at these large galactocentric radii, the majority of stars are quite enriched, with peaks in the MDFs shifting from [Z/H] ~ -0.5 at 15 kpc to [Z/H] ~ -0.65 at 60 kpc.

All three fields have a tail of stars extending to low metallicities. We find that the mean metallicity and the ratio of metal-poor to metal-rich stars increase significantly with galactocentric radius. We detect a distinct metal-poor population 4σ above the low-metallicity tail in the inner and outer fields. This is apparent as a second peak in the MDF at [Z/H] ~ -1.3. The reason for the absence of this peak in the middle field is uncertain, but we suggest that substructure is the likely cause. This second peak is consistent with hierarchical halo formation theories that predict a relatively low concentration metal-poor halo that becomes increasingly significant at larger radii. By extrapolating the stellar density profiles observed, we estimate the total stellar mass of NGC 3115's metal-poor halo to be in the range $(1 < M_* < 4) \times 10^{10} M_\odot$ (∼14% of the galaxy's total stellar mass).

The stellar halo compares well with the expectations from NGC 3115's globular cluster population. The densities of halo stars and globular clusters appear to decrease in a similar fashion with increasing radius, such that the metal-poor population has a shallower profile than the metal-rich population. The low-metallicity peak observed at [Z/H] ~ -1.3 in the stellar population is likely associated with the metal-poor globular cluster population. This is the strongest evidence to date that globular clusters trace the stellar populations in the halos of early-type galaxies. However, the fraction of metal-poor to metal-rich globular clusters is much higher than that of the stars. This is similar to the difference observed in the Milky Way. The relatively large number of globular clusters associated with the metal-poor stellar halo, as well as the fact that the globular clusters are found to have a similar metallicity and profile to the metal-poor stars, supports their use as bright chemodynamical tracers of the stellar halos of more distant galaxies.

Future *HST* observations of more fields in NGC 3115's outer halo will be important in improving our knowledge. By covering more area, we can test for substructure in the halo and detect more stars in the low-density outer regions, thereby increasing the significance of our conclusions. Of particular importance will be more distant observations in NGC 3115's halo, beyond 100 kpc, where the metal-poor halo is projected to be more dominant. In addition, integrated surface brightness photometry of the stellar halo of NGC 3115 at large radii would be powerful in comparing with our stellar population analysis. Such observations would allow us to test for substructure in NGC 3115's halo.

This work is supported in part by HST-GO-13048.01, HST-GO-13048.002-A, and National Science Foundation grant AST-1211995. This research has made use of NASA's Astrophysics Data System. We also made use of the up-to-date python/pyraf/stsdas tasks installed using the Ureka package (http://ssb.stsci.edu/ureka/). M.B.P. thanks the STSci Ureka helpdesk for assistance with an issue running the tweakshift task installed by this package on Mac OSX.

APPENDIX

THE EFFECT OF STELLAR LUMINOSITY RANGE ON THE DERIVED MDFS

To construct MDFs of the observed stellar populations, we must choose which regions of the CMDs to study. This choice is nontrivial. We wish to include as many stars as possible while only including those stars with reliable color–magnitude (and hence metallicity) information. In Figure 15 we investigate how the choice of different magnitude limits affects the resulting MDFs. These cuts go down to F110W = 26.5, where the average error on the F606W−F110W color is $\lesssim$0.15. The region of the CMD studied is indicated in the insert of each panel. The left panels consider simple cuts based on the F110W magnitude of the stars. The right panel takes F110W magnitude cuts relative to the TRGB magnitude, noting that this varies as a function of metallicity. It can be seen that, while some variation is observed as a result of the cuts chosen, the general features of the MDFs—i.e., the location of the primary and secondary peaks—are quite robust to this choice.

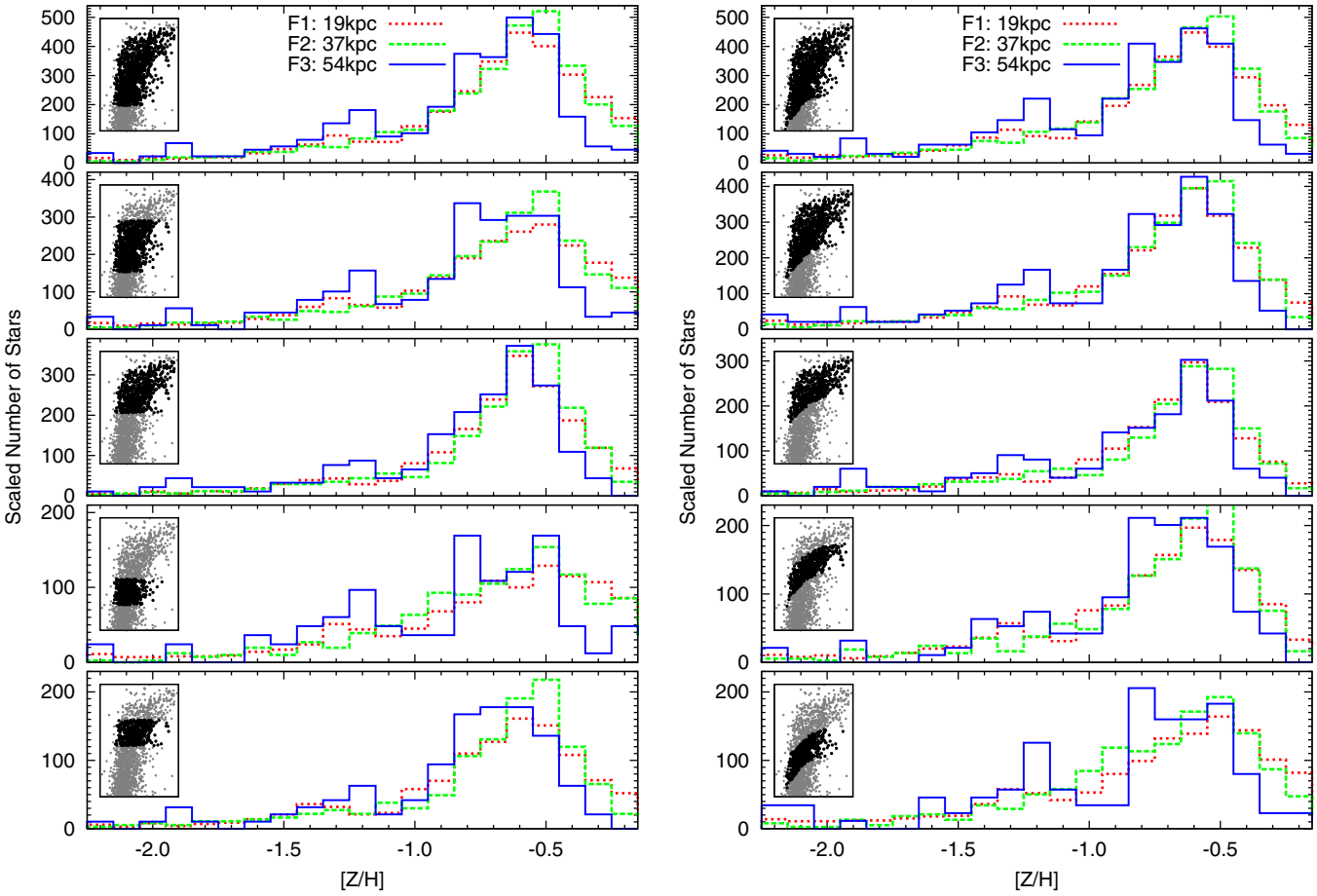

Figure 15. Metallicity distributions of stars in fields F1 (red dotted line), F2 (green dashed line), and F3 (blue solid line), scaled to have the same total number of stars as F1. The different panels adopt different magnitude cuts for stars used to construct the histograms. The left panels consider stars within F110W magnitude cuts. The right panels consider stars with magnitude cuts relative to the TRGB for their measured metallicity. The inserts are CMDs for the F2 field (gray), with the stars included in the MDF highlighted in black. It can be seen that the choice of magnitude cut has little effect on the characteristics of the MDFs in each field. We restrict our analysis of the MDFs to [Z/H] < -0.15—at higher metallicities, the MDFs become increasingly unreliable owing to incompleteness.

REFERENCES

Abraham, R. G., & van Dokkum, P. G. 2014, PASP, 126, 55
Arnold, J. A., Romanowsky, A. J., Brodie, J. P., et al. 2011, ApJL, 736, L26
Bassino, L. P., Faifer, F. R., Forte, J. C., et al. 2006, A&A, 451, 789
Bell, E. F., Zucker, D. B., Belokurov, V., et al. 2008, ApJ, 680, 295
Bica, E., Bonatto, C., Barbuy, B., & Ortolani, S. 2006, A&A, 450, 105
Binney, J., & Merrifield, M. 1998, Galactic Astronomy (Princeton, NJ: Princeton Univ. Press)
Brodie, J. P., Romanowsky, A. J., Strader, J., et al. 2014, ApJ, 796, 52
Brodie, J. P., & Strader, J. 2006, ARA&A, 44, 193
Brodie, J. P., Usher, C., Conroy, C., et al. 2012, ApJL, 759, L33
Bullock, J. S., & Johnston, K. V. 2005, ApJ, 635, 931
Cantiello, M., Blakeslee, J. P., Raimondo, G., et al. 2014, A&A, 564, L3
Capaccioli, M., Held, E. V., & Nieto, J.-L. 1987, AJ, 94, 1519
Cardelli, J. A., Clayton, G. C., & Mathis, J. S. 1989, ApJ, 345, 245
Carollo, D., Beers, T. C., Chiba, M., et al. 2010, ApJ, 712, 692
Ciardullo, R., Feldmeier, J. J., Jacoby, G. H., et al. 2002, ApJ, 577, 31
Cooper, A. P., Cole, S., Frenk, C. S., et al. 2010, MNRAS, 406, 744
Cooper, A. P., D'Souza, R., Kauffmann, G., et al. 2013, MNRAS, 434, 3348
Courteau, S., Widrow, L. M., McDonald, M., et al. 2011, ApJ, 739, 20
Dalcanton, J. J., Williams, B. F., Melbourne, J. L., et al. 2012, ApJS, 198, 6
Dolphin, A. E. 2000, PASP, 112, 1383
Dotter, A., Chaboyer, B., Jevremović, D., et al. 2008, ApJS, 178, 89
D'Souza, R., Kauffman, G., Wang, J., & Vegetti, S. 2014, MNRAS, 443, 1433
Elson, R. A. W. 1997, MNRAS, 286, 771
Fall, S. M., & Romanowsky, A. J. 2013, ApJL, 769, L26
Forbes, D. A., Spitler, L. R., Strader, J., et al. 2011, MNRAS, 413, 2943
Gilbert, K. M., Kalirai, J. S., Guhathakurta, P., et al. 2014, ApJ, 796, 76
Girardi, L., Williams, B. F., Gilbert, K. M., et al. 2010, ApJ, 724, 1030
Guarnieri, M. D., Renzini, A., & Ortolani, S. 1997, ApJL, 477, L21
Harris, W. E., & Harris, G. L. H. 2002, AJ, 123, 3108
Harris, W. E., Harris, G. L. H., Layden, A. C., & Stetson, P. B. 2007a, AJ, 134, 43
Harris, W. E., Harris, G. L. H., Layden, A. C., & Wehner, E. M. H. 2007b, ApJ, 666, 903
Ibata, R., Irwin, M., Lewis, G., Ferguson, A. M. N., & Tanvir, N. 2001a, Natur, 412, 49
Ibata, R., Irwin, M., Lewis, G. F., & Stolte, A. 2001b, ApJL, 547, L133
Ibata, R., Mouhcine, M., & Rejkuba, M. 2009, MNRAS, 395, 126
Ibata, R. A., Lewis, G. F., McConnachie, A. W., et al. 2014, ApJ, 780, 128
Jarrett, T. H., Chester, T., Cutri, R., Schneider, S. E., & Huchra, J. P. 2003, AJ, 125, 525
Jennings, Z. G., Strader, J., Romanowsky, A. J., et al. 2014, AJ, 148, 32
Kirby, E. N., Cohen, J. G., Guhathakurta, P., et al. 2013, ApJ, 779, 102
Kirby, E. N., Lanfranchi, G. A., Simon, J. D., Cohen, J. G., & Guhathakurta, P. 2011, ApJ, 727, 78
Kundu, A., & Whitmore, B. C. 1998, AJ, 116, 2841
Kundu, A., & Whitmore, B. C. 2001, AJ, 122, 1251
La Barbera, F., Ferreras, I., de Carvalho, R. R., et al. 2012, MNRAS, 426, 2300
Lebzelter, T., Nowotny, W., Hinkle, K. H., Höfner, S., & Aringer, B. 2014, A&A, 567, A143
Lee, M. G., Freedman, W. L., & Madore, B. F. 1993, ApJ, 417, 553
Lynden-Bell, D. 1975, VA, 19, 299
Marigo, P., Girardi, L., Bressan, A., et al. 2008, A&A, 482, 883
Martínez-Delgado, D., Gabany, R. J., Crawford, K., et al. 2010, AJ, 140, 962
Mihos, J. C., Harding, P., Spengler, C. E., Rudick, C. S., & Feldmeier, J. J. 2013, ApJ, 762, 82
Monachesi, A., Bell, E. F., Radburn-Smith, D. J., et al. 2013, ApJ, 766, 106
Norris, M. A., Sharples, R. M., & Kuntschner, H. 2006, MNRAS, 367, 815
Pagel, B. E. J. 1997, Nucleosynthesis and Chemical Evolution of Galaxies (Cambridge: Cambridge Univ. Press)

Peng, E. W., Jordán, A., Côté, P., et al. 2006, ApJ, 639, 95
Prantzos, N., & Silk, J. 1998, ApJ, 507, 229
Radburn-Smith, D. J., de Jong, R. S., Seth, A. C., et al. 2011, ApJS, 195, 18
Rejkuba, M., Greggio, L., Harris, W. E., Harris, G. L. H., & Peng, E. W. 2005, ApJ, 631, 262
Rejkuba, M., Harris, W. E., Greggio, L., & Harris, G. L. H. 2011, A&A, 526, A123
Rejkuba, M., Harris, W. E., Greggio, L., et al. 2014, ApJL, 791, L2
Renzini, A. 1998, AJ, 115, 2459
Rich, R. M. 1990, ApJ, 362, 604
Robin, A. C., Reylé, C., Derrière, S., & Picaud, S. 2003, A&A, 409, 523
Salaris, M., Chieffi, A., & Straniero, O. 1993, ApJ, 414, 580
Schlafly, E. F., & Finkbeiner, D. P. 2011, ApJ, 737, 103
Schlesinger, K. J., Johnson, J. A., Rockosi, C. M., et al. 2012, ApJ, 761, 160
Schmidt, M. 1963, ApJ, 137, 758
Searle, L., & Zinn, R. 1978, ApJ, 225, 357
Spitler, L. R. 2010, MNRAS, 406, 1125
Strader, J., Brodie, J. P., Spitler, L., & Beasley, M. A. 2006, AJ, 132, 2333
Talbot, R. J., Jr., & Arnett, W. D. 1971, ApJ, 170, 409
Taylor, M. B. 2006, in ASP Conf. Ser. 351, Astronomical Data Analysis Software and Systems XV, ed. C. Gabriel, C. Arviset, D. Ponz, & S. Enrique (San Francisco, CA: ASP), 666
Tonry, J. L., Dressler, A., Blakeslee, J. P., et al. 2001, ApJ, 546, 681
Usher, C., Forbes, D. A., Brodie, J. P., et al. 2012, MNRAS, 426, 1475
van den Bergh, S. 1962, AJ, 67, 486
van Dokkum, P. G., Abraham, R., & Merritt, A. 2014, ApJL, 782, L24
Woolf, V. M., & West, A. A. 2012, MNRAS, 422, 1489
Worthey, G., Dorman, B., & Jones, L. A. 1996, AJ, 112, 948
Wu, P.-F., Tully, R. B., Rizzi, L., et al. 2014, AJ, 148, 7
Zolotov, A., Willman, B., Brooks, A. M., et al. 2010, ApJ, 721, 738